

SPARSITY ENHANCED RECONSTRUCTION METHODS FOR DIFFUSE
OPTICAL TOMOGRAPHY

by
JIXING YAO

Presented to the Faculty of the Graduate School of
The University of Texas at Arlington in Partial Fulfillment
of the Requirements
for the Degree of

DOCTOR OF PHILOSOPHY

THE UNIVERSITY OF TEXAS AT ARLINGTON

December 2013

Copyright © by Jixing Yao 2013
All Rights Reserved

ACKNOWLEDGEMENTS

First and foremost, I would like to express my earnest gratitude to my supervisor, Prof. Soontorn Oraintara, for constantly inspiring and encouraging me, and also for his invaluable advice and limitless patience during the course of my doctoral study. I really appreciate his profound insights and excellent guidance toward research which have led me finish this work. I would like to thank Prof. Hanli Liu for her supports on the experimental data and comments on my research results. I want to thank my committee members, Prof. Michael T. Manry, Prof. Qilian Liang, and Prof. Ioannis D. Schizas, for their interest in my research and for taking time to serve in my dissertation committee. I take this opportunity to express my gratitude to all of my teachers who have ever taught me for shaping my knowledge and attitudes.

I would like to give my sincere thanks to my MSP Lab friends, Dr. Yothin Rakvongthai, Dr. Nha Nguyen, Dr. Truong Nguyen, Lakshmi Srinivasan, Srikanth Sathyanarayanan, and Tanmoy Bhowmik as well as a group of friends in the Bioengineering Department at UTA for their support and fruitful discussions on my research. Special acknowledgement goes to Dr. Yothin Rakvongthai for his help when I first started my PhD program and for the collaboration on the relative noise model, which has played an important role in this dissertation. Furthermore, I would like to thank several of my friends for their friendship and also for making my life here more delightful.

Last but most importantly, I would like to offer my deepest gratitude to my parents whose constant encouragement and support have really brought me here.

November 15th, 2013

ABSTRACT

SPARSITY ENHANCED RECONSTRUCTION METHODS FOR DIFFUSE OPTICAL TOMOGRAPHY

Jixing Yao, Ph.D.

The University of Texas at Arlington, 2013

Supervising Professor: Soontorn Orintara

Conventional reconstruction algorithms for diffuse optical tomography (DOT) is based on Tikhonov regularization method and the simple white Gaussian noise (WGN) assumption. These approaches usually lead to the following problems: 1. The reconstructed images are blurry; 2. In 3D reconstruction problems, the reconstructed objects are usually in the wrong depths; 3. The shape of a reconstructed object might be different from its original one due to the noise.

In this work, after study the nature of DOT images as well as the data acquisition process, several sparsity regularization related reconstruction methods were developed to improve the spatial resolution as well as the fidelity of the reconstructed image. First, this thesis presents a simple reconstruction formula that adjusts the sensing matrix to improve the depth reconstruction in the 3D space. With the sparsity constraint, the spatial resolutions of a reconstructed image can also be improved even with WGN added to the measurements.

Next, to make the reconstruction formula more practical, the physical sensing model and its relationship with the measurement noise are further studied. Conse-

quently, an effective noise quantification method is derived. By incorporating this noise level information to the reconstruction process, objects with more complex shapes can be recovered almost correctly.

Finally, the relative noise (RN) model is derived by considering the transformation from the light intensity measurements to relative light density changes. Thereafter, a maximum a posteriori (MAP) estimator, together with both ℓ_1 norm and ℓ_2 norm regularization terms, is developed. The resulting optimization problem is solved by the ellipsoid algorithm. The improvement of using this more accurate noise model is demonstrated by both computer simulation and phantom experiments.

TABLE OF CONTENTS

ACKNOWLEDGEMENTS	iii
ABSTRACT	iv
LIST OF FIGURES	ix
LIST OF TABLES	xii
Chapter	
1. INTRODUCTION	1
1.1 Forward Model	3
1.2 Inverse Problem	5
1.3 Problem Statement	6
1.4 Thesis Outline	7
2. 3D DOT RECONSTRUCTION WITH SPARSITY CONSTRAINT	8
2.1 Sparsity Regularized DOT Reconstruction	10
2.2 The Depth of 3D DOT Reconstruction	16
2.3 Experimental Results	21
2.3.1 Computer Simulation	21
2.3.2 Laboratory Experiment	21
2.4 Conclusion	23
3. IMPROVED RECONSTRUCTION WITH RELATIVE NOISE APPROX- IMATION	26
3.1 Approximation of The Relative Noise	27
3.1.1 Noise Analysis	28
3.1.2 Noise Variance Quantification	30

3.1.3	Numerical Validation	33
3.1.4	Noise Quantification Assisted DOT Image Inversion	35
3.2	Experimental Results	36
3.2.1	Computer Simulation	36
3.2.2	Laboratory Experiment	40
3.2.3	Human Finger Tapping Experiment	46
3.3	Conclusion	48
4.	DOT RECONSTRUCTION WITH THE RELATIVE NOISE MODEL . .	50
4.1	The Relative Noise Model	50
4.1.1	RN Model Based Reconstruction Formula	51
4.2	Optimization Problem	56
4.3	Experimental Results	58
4.3.1	Simulated Data	59
4.3.2	Phantom Data	62
4.3.3	Parameter Selection	64
4.4	Conclusion	65
5.	SUMMARY AND FUTURE DIRECTIONS	66
5.1	Summary	66
5.2	Future Directions	67
5.2.1	Improve the Reconstruction Speed of RN Model Formula . . .	67
5.2.2	Combine the Physiological Noise Into the RN Model	68
5.2.3	Develop a More Effective Method to Find the Optimal Reg- ularization Parameters When Both ℓ_1 Norm and ℓ_2 Norm are Used	68
Appendix		
A.	Acronyms	70

B. Derivation of RN pdf When Both Inhomogeneous and Background Measure- ments Are Corrupted by Noise	73
C. Implementation of the Ellipsoid Algorithm	79
REFERENCES	82
BIOGRAPHICAL STATEMENT	93

LIST OF FIGURES

Figure	Page
1.1 The absorption spectra of oxygenated and deoxygenated hemoglobin in the near infrared range	1
2.1 An example of the L curve	12
2.2 Geometry of the simulation and phantom experiments	14
2.3 The original image (a) and the reconstructed images obtained using (b) Tikhonov method and (c) SIRA	15
2.4 Reconstructed images obtained using (a) Tikhonov method and (b) SIRA in log scale	16
2.5 Original image for the 3D reconstruction simulation	17
2.6 Reconstruction results of the 3D reconstruction simulations with (a) Tikhonov methods and (b) SIRA	18
2.7 Measurement sensitivity when light propagates from one source to one detector	19
2.8 3D Reconstruction of simulation data with a spherical object located at 2 cm below the S-D plane. (a) the x - y plane at different depth. (b) x - z plane when $y = 0$	22
2.9 3D Reconstruction of phantom data with a spherical object located at 2 cm below the S-D plane. (a) the x - y plane at different depth. (b) x - z plane when $y = -0.6$	24
3.1 Noise variance of different S-D pairs in a laboratory phantom experiment	28

3.2	Comparison between the actual noise variance and the estimated noise variance	34
3.3	The original image used for the simulation	37
3.4	Comparison of the reconstructions with:(a)Tikhonov (b) GLS; (c) SIRA; (d) SIRANN	38
3.5	Calculated SNRs among different channels in the phantom experiment	41
3.6	Reconstructed images obtained by using (a) Tikhonov method, (b) SIRA, and (c) SIRANN with derived noise quantification method . . .	43
3.7	Vertical cross sections of reconstructions from SIRA, SIRANN, and Tikhonov method	44
3.8	Absorber used in the second phantom experiment	44
3.9	The reconstructed image of the phantoms experiment by (a) Tikhonov, (b) GLS, (c)SIRA, and (c) SIRANN method	45
3.10	The reconstructed image of the phantoms experiment with measurements from the first to seventh nearest S-D pairs by (a) SIRA, and (b) proposed improving method	46
3.11	Source detector geometry of the finger tapping experiment	48
3.12	Reconstructed images of the finger tapping experiment using (a) Sparsity regularization (b) SIRANN method with the proposed noise model	49
4.1	Comparison of the derived RN pdf and Gaussian pdf with normalized histogram generated from 10^6 samples	52
4.2	The unit circle of ℓ_1 norm (in red dash line), ℓ_2 norm (in black dot-dash line), and the combination of both ℓ_1 norm and ℓ_2 norm (in solid blue line)	53
4.3	An example of the RN cost function with $x \in \mathbb{R}^2$	57

4.4	(a) The original image used for the simulation, and comparison of the reconstructions with:(b)Tikhonov; (c)LSL12; (d) RN estimator.	60
4.5	Cross section profile of reconstructions from LSL12, RN, and Tikhonov method	61
4.6	Reconstructions of phantom experimental data by:(a)Tikhonov (b)LSL12; (b)RN estimator.	64

LIST OF TABLES

Table		Page
3.1	SSIM and CNR values of simulation reconstructions with Tikhonov, GLS, SIRA, and SIRANN.	39
3.2	SSIM and CNR values of phantom reconstructions with Tikhonov, GLS, SIRA, and SIRANN method from 188 measurements as well as with SIRA and SIRANN method from 220 measurements.	47
4.1	SSIM and CNR values of simulation reconstructions with Tikhonov, LSL12, and proposed RN estimator.	62
4.2	SSIM and CNR values of phantom reconstructions with LSL12, and proposed RN estimator.	65

CHAPTER 1

INTRODUCTION

The diffuse optical tomography (DOT) is one of the emerging noninvasive medical imaging technique, which uses low power light in the near infrared (NIR) range to detect the differences of optical properties inside the human body. In particular, the absorption spectra of oxygenated hemoglobin (HbO) and deoxygenated hemoglobin (Hb) at the NIR wavelength differ markedly as shown in Fig.1.1.

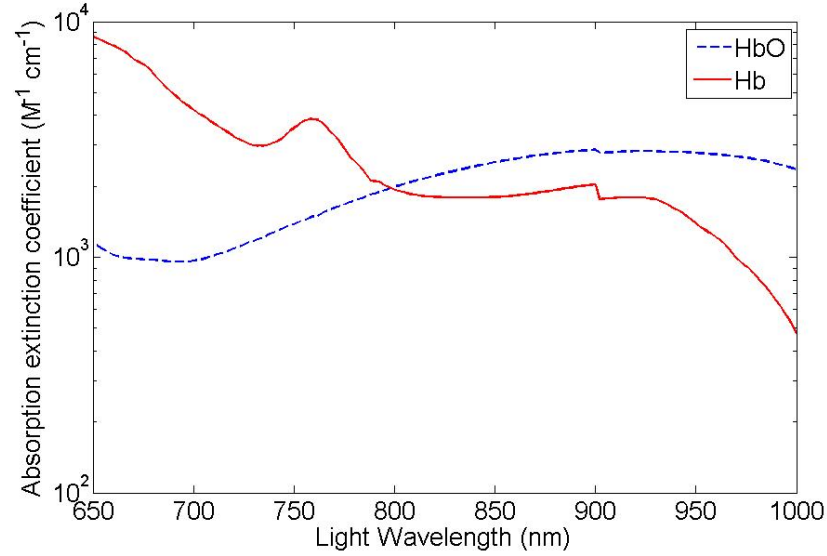


Figure 1.1. The absorption spectra of oxygenated and deoxygenated hemoglobin in the near infrared range.

As a result, the oxygen density in particular areas can be detected by taking measurements at different light wavelengths within the near infrared range.

Despite the limitation of spatial resolution and depth penetration as compared to magnetic resonance imaging (MRI) or computed tomography (CT), the DOT technique provides generally a cheaper and more portable imaging solution, together with higher temporal resolution. Recently, this has gained considerable interests and become an important tool for medical imaging [37], and has been used for the applications such as functional brain imaging [10, 72] and cancer detection [19, 61].

Generally speaking, the DOT imaging systems can be categorized into three different types: frequency-domain systems, time-domain systems, and continuous-wave (CW) systems [8]. For the frequency-domain imaging, the light sources are amplitude modulated (AM). The images can be obtained from the phase delay information of the measured AM light. The time-domain system, on the other hand, implements a short light pulse as the input signal. In this case, the detected output signal can be considered as the impulse response of the medium. Because when the injected light traveling through the medium, the photons are actually traveling via different reflection paths, which results different time delays. At the end, the CW system can actually be considered as a special case of the frequency-domain systems, where the modulation frequency is set to zero. Hence the CW systems can only detect the magnitude attenuation of the input signal. Among these three types of systems, the CW systems are the simplest and the cheapest. As a result, the CW systems are widely accepted by the DOT community [12], and is the kind of system focused in this research.

Moreover, depending on the applications, a variety of geometries have also been used for the DOT system. For example, (1) the planar geometry: sources and detectors are placed either on the same plane or on two parallel planes; (2) the cylindrical geometry: sources and detectors are located on the boundary of the cylinder and usually with the assumption that the cylinder is infinitely long; (3) the

spherical geometry: sources and detectors are scattered over the surface of the sphere. In this work, among all those geometries, we study the one that is widely used for the human brain function imaging applications [10, 72]. For this scenario, sources and detectors are placed on the same plane, and only reflective lights are detected. During the detecting process, sources are turned on one after another. At the mean time the reflective light densities are observed by all the detectors, and recorded as the measurements. In other words, measurements are collected from the pairs formed by different sources and different detectors. At the end, all the available measurements or a number of selected measurements are used to reconstruct the image.

A medical imaging problem can be generally divided into two sub-problems: the forward problem, which deals with the physical model of the imaging system, and the inverse problem, which converts the measurements into an image [5]. The fundamental forward model as well as the conventional inversion technique for the DOT problems are discussed in the next two sub-sections.

1.1 Forward Model

Before reconstructing the image from the measured data, investigating the forward physical model is necessary since an accurate forward model is the key to find a correct reconstruction. When light propagates in biological media, scattering and absorption are two fundamental interactions between light and tissue. Given that the reduced scattering coefficient is much greater than the absorption coefficient for near infrared light, this process can be modeled as the diffusion approximation (DA) of the Boltzmann transport equation [60]. The DA of the frequency domain system is given by:

$$-\nabla \cdot D(\mathbf{r})\nabla\Phi(\mathbf{r},\omega) + c\mu_a(\mathbf{r})\Phi(\mathbf{r},\omega) + j\omega\Phi(\mathbf{r},\omega) = cS(\mathbf{r},\omega), \quad (1.1)$$

where c is the speed of light in the medium, S is the isotropic source providing the number of photons emitted at position \mathbf{r} , and Φ is the photon fluence rate. D is the diffusion coefficient, which is defined as $D = c/3(\mu_a + \mu'_s)$, where μ'_s is the reduced scattering coefficient defined as $\mu'_s = (1 - g)\mu_s$ and g is the averaged cosine of the scattering angle. Moreover, since in most of the tissues $\mu'_s \gg \mu_a$, $D \approx c/(3\mu'_s)$. The DA of cw system can be obtained from (1.1) by setting $\omega = 0$, since the cw system can be considered as a special frequency domain system with the frequency $\omega = 0$.

The forward solution of (1.1) can be obtained by applying the Monte Carlo methods [9, 32], finite element method [6, 68], finite difference method [2, 65], random walk method [34, 35], and linear Born/Rytov approximation [4, 63, 67] etc.

In general, Eq. (1.1) governs light propagation and distribution in tissues as a function of tissue optical properties, namely, light scattering and absorption. However, this study focuses only on functional brain imaging, with the assumption that the change in light scattering is small [10, 28]. Thus, changes of light scattering induced by brain activation can be ignored without causing significant errors. Consequently, the forward solution of (1.1) can be solved by the linear Rytov approximation [64]. After combining with the modified Beer-Lambert law [23], the Rytov approximation yields the following equation[10]:

$$\ln \frac{\Phi_0(\mathbf{r}_d, \mathbf{r}_s)}{\Phi(\mathbf{r}_d, \mathbf{r}_s)} = \Delta_{\mu_a} L, \quad (1.2)$$

where Δ_{μ_a} is the relative absorption change from a source at position \mathbf{r}_s to a detector at position \mathbf{r}_d between two measurement states, Φ_0 and Φ , L is the average optical path length of light propagating through the medium, $\Phi_0(\mathbf{r}_d, \mathbf{r}_s)$ is related to the baseline measurements or the background measurements. Therefore, the left hand side of (1.2) can be considered as the measured relative light density changes or the relative measurements.

1.2 Inverse Problem

Eq. (1.2) can be further discretized into the following linear equation:

$$\mathbf{Ax} = \mathbf{b}, \quad (1.3)$$

where $\mathbf{b} \in \mathbb{R}^{M \times 1}$ is the vector of measured relative light density changes from M different source-detector (S-D) pairs, $\mathbf{x} \in \mathbb{R}^{N \times 1}$ is the vector being related to the changes of absorption properties in spatial domain and discretized into voxels (i.e. $x_i = \delta_{\mu(x_i)}$), and $\mathbf{A} \in \mathbb{R}^{M \times N}$ is the sensing matrix referring to the sensitivity of voxels with respect to different S-D pairs.

Due to the limited numbers of sources and detectors, the number of measurements obtained is much fewer than that of voxels to be reconstructed. As a result, the \mathbf{A} matrix is highly ill-posed and the solution of (1.3) is not unique [77]. Therefore regularization to the solutions is required. The conventional way to regularize the solution is to use $\|\mathbf{x}\|_2$, which is the ℓ_2 norm of \mathbf{x} , as defined by $\|\mathbf{x}\|_2 = \sqrt{\sum_i |x_i|^2}$. This approach is also known as the Tikhonov regularization method [75], where the image can be reconstructed from the following equation:

$$\begin{aligned} \hat{\mathbf{x}} &= \arg \min_{\mathbf{x}} \{ \|\mathbf{Ax} - \mathbf{b}\|_2^2 + \lambda \|\mathbf{x}\|_2^2 \} \\ &= \mathbf{A}^T (\mathbf{AA}^T + \lambda \mathbf{I})^{-1} \mathbf{b}, \end{aligned} \quad (1.4)$$

where \mathbf{A}^T denotes the transpose of \mathbf{A} , and λ is the regularization parameter that controls the balance between the data fidelity and regularization terms. Methods of selecting this parameter for the optical imaging problem have been discussed extensively in [20]. The Tikhonov method is simple and easy to implement, and therefore is widely used.

Besides solving the linear equations in (1.3), many other reconstruction methods were also proposed. For example, the series papers of inverse problem in optical

diffusion tomography by Markel et al.[54, 55, 56, 57] were based on solving (1.2) directly. Yet, these kinds of inversion formulas are outside the scope of this work and are not discussed.

1.3 Problem Statement

Similar to many other medical imaging applications, reconstructing high quality images from a limited number of measurements is one of the main challenges. Specifically in the DOT problems, improving the quality of the reconstructed images is one of the main challenges. DOT images often appear less spatial resolution as compared to other medical imaging modalities (e.g., CT or MRI). The poor spatial resolution in DOT stems from the scattering nature of light traveling in tissue, leading to a low signal-to-noise ratio (SNR), particularly when the source and detector separation is large (3-4 cm). Moreover, the sensing operator of DOT is usually ill-posed. As a result, infinitely many solutions exist and the solutions are sensitive to the measurement noise [41, 66, 77]. Hence, an appropriate regularization method is required to find the correct solution, and the analysis of noise is needed to increase the robustness of the reconstruction algorithm.

A variety of solutions have been proposed and explored to improve the quality of DOT reconstructions by (1) optimally selecting optode arrangements to boost the SNR and gain more information from the measurements, as discussed in [72, 21, 50], (2) increasing the density of sources and detectors to increase the number measurements and therefore enhance the spatial resolution of reconstructed images [30, 33], (3) applying different regularization terms in image reconstruction algorithms based on prior information and different properties of the images to be reconstructed, which eventually improve the quality of reconstruction results [27, 14, 50], and (4) incorporating prior information obtained from other imaging modalities to define

the positions and shapes of the objects to be recovered[40, 26, 51]. Furthermore, algorithms targeting each individual type of the DOT systems [62, 15] or different types of statistical models [14, 62] are also showing promising results.

In this work, following aspects of the DOT reconstruction problem were investigated:

1. the features of DOT images and how to fit these features into the compressive sensing (CS) framework;
2. the properties of the sensing matrix and how it relates to the image distortion;
3. the forward model and its relationship to the instrument noise; and
4. how to effectively reduce the measurement noise in the reconstruction process.

1.4 Thesis Outline

Chapter 2 introduces sparsity regularized 3D reconstruction algorithm. The relative noise (RN) is introduced and a reconstruction method based on the approximation of RN term are derived in Chapter 3. A more precise RN model as well as the corresponding reconstruction formula are discussed in Chapter 4. Summary and possible future directions are discussed and listed in Chapter 5.

CHAPTER 2

3D DOT RECONSTRUCTION WITH SPARSITY CONSTRAINT

In this chapter, the features of DOT images as well as the sensing matrix were investigated and corresponding algorithms were developed.

As shown in (1.4), the conventional way to solve the DOT problem is to use the ℓ_2 norm of the image as the regularization term. However, using only the ℓ_2 norm of the image as the regularization term over-penalizes pixels with large coefficients and produces many pixels with unwanted small coefficients. This tends to blur the reconstructed images and results in poor spatial resolution. As a result, the reconstructed object in a DOT image often appears low spatial resolution and unclear boundary, as compared to other medical imaging modalities (e.g., CT or MRI). Hence, one of the main challenges in DOT is to improve the spatial resolution of the reconstructed images. In general, many images in DOT problems are usually sparse, i.e., most of the coefficients in \mathbf{x} are zero or close to zero. Especially in the application of functional brain imaging [10], a reconstructed DOT image reflects only the relative changes in absorption coefficient within the field of view (FOV) between two different time instances or before and after concentration change, and most likely the active areas are relatively small compared to the entire measured regions interrogated by the optical probe array. Also, the oscillation in the background is small or close to zero. In the application of cancer detection [18, 19], the lesion is also smaller than the normal tissue.

Taking into account the sparseness of a DOT image, several methods have been proposed to improve the spatial resolution of the reconstructions [50, 14, 70, 45].

In [14], an algorithm using ℓ_1 norm regularization has been applied for the DOT problem. Therein, the expectation maximization (EM) algorithm is employed to solve the following optimization:

$$\hat{\mathbf{x}} = \arg \max_{\mathbf{x}} \{\ln p(\mathbf{b}|\mathbf{x}) - \lambda \|\mathbf{x}\|_1\},$$

where $p(\mathbf{b}|\mathbf{x})$ is the conditional probability distribution function (pdf) of \mathbf{b} given \mathbf{x} . Compared to the Tikhonov regularization, the results yielded by this method demonstrate better spatial resolution. However, applying the EM algorithm requires statistical information of the measurements in order to solve the inverse problem. Such information is easy to find in simulations, but can be difficult for real implementations due to the diversity of devices and measuring environments. Furthermore, the compressed sensing concept was first introduced in [70], where the authors mapped the image into the frequency domain and yielded the following cost function:

$$\hat{\mathbf{x}} = \arg \min_{\mathbf{x}} \{\|\mathbf{A}\mathbf{x} - \mathbf{b}\|_2^2 + \lambda \|\mathcal{F}(\mathbf{x})\|_1\},$$

where \mathcal{F} represents the Fourier transform. Hence the regularization term in this method is the Fourier coefficients of the image under the assumption that the image is sparse in its frequency domain. This assumption might be true for certain images, but as we mentioned the images in DOT are usually sparse in the spatial domain. In general, the sparse spatial domain signal is not sparse in its frequency domain. As a result using the ℓ_1 norm of image's Fourier coefficients as a regularization term can only yield blurred images. Regularization with the total variation (TV) as well as the Hubert function were discussed in [27], where the edges of the targets are better preserved. However, these methods are only suitable for piecewise constant images. Sparseness of the DOT image in the spatial domain and an ℓ_0 norm based compressive sensing algorithm were discussed in [50], with a major challenge of its

non-convexity. Recently, a combination of the ℓ_1 regularization and the Depth Compensation Algorithm (DCA) has been reported in [45], which shows an improvement in both the spatial resolution and the depth localization in the 3D DOT reconstruction. A method of preconditioning the sensing matrix was discussed in [43], which can be used to improve compressive sensing based reconstruction methods.

In addition, the limitation of using only the ℓ_1 norm regularization is that the cardinality of original image coefficient should be less than the average number of sources and detectors [50]. However, in regular DOT applications the number of optodes is usually a small number. Hence using only the ℓ_1 norm might yield results that are over-sparse. To concur this limit, the straightforward way is to decrease the image resolution or increase the pixel size, so the the cardinality of the image is reduced. On the other hand, several methods have been proposed to break the limit while maintain the same resolution. The concept of group lasso or group sparsity is intend to partition the images into several groups, then the sum of the ℓ_2 norm of each group is used to regularize the solution, i.e. the so call $\ell_{2,1}$ norm[42, 49, 58]. The authors of [82] suggested that using both ℓ_1 norm and ℓ_2 norm at the same time as a regularizer is also an effective choice to improve the spatial quality without over-sparse the reconstructed images.

2.1 Sparsity Regularized DOT Reconstruction

For sparse images, it is desired to use the ℓ_1 norm of image coefficients as the regularization term[13]. Hence, we first suggest to utilize the sparse image reconstruction algorithm (SIRA) for the DOT problem by replacing the ℓ_2 norm of \mathbf{x} in

(1.4) with a sparsity regularization term. The image reconstruction task now becomes solving the following equation [53]:

$$\hat{\mathbf{x}} = \arg \min_{\mathbf{x}} \{\|\mathbf{Ax} - \mathbf{b}\|_2^2 + \lambda \|\mathbf{x}\|_1\}. \quad (2.1)$$

A high quality reconstruction also relies on the selection of regularization parameter λ . Because the regularization parameter controls the smoothness of the result, a wrong choice of such a parameter could lead to an incorrect image. Especially for clinical applications, a wrong image might lead to improper diagnoses. Numbers of parameter selection methods have been developed for the Tikhonov regularization such as the L-curve method[41] and the generalized cross-validation(GCV) [38]. The L-curve method is based on the fact that the log-log plot of $\|Ax - b\|_2$ vs $\|x\|_2$ often has an “L” shape and the optimal parameter can be found near the so call L-corner as shown in Fig. 2.1. In general, the L-curve can be found in most of the regularized optimization problems by plotting the log-log figure of the fidelity term vs the regularization term. Hence it can also be used for the sparsity regularized reconstruction formula in (2.1). Similarly, the GCV method has successfully used for many ℓ_1 norm regularization applications. Unfortunately, for a smaller data set, i.e. the number of measurements is much smaller than the number of voxels, this method is unstable and often results in under-smoothing. As a result, the GCV method cannot be implemented to find an optimal regularization parameter in the DOT problem. Besides these two methods, a simple method called the quasi-optimality principle has also been proved can be used to select the regularization parameter with sparsity regularization[44]. The optimal choice of the parameter λ_* is simply defined as:

$$\lambda_* = \arg \min_{\lambda} \|\hat{x}_{\lambda_n} - \hat{x}_{\lambda_{n+1}}\|, \quad (2.2)$$

where $\lambda_n = \lambda_0 * q^n, 0 < q < 1$ and \hat{x}_{λ_n} is the reconstructed result with regularization parameter set to λ_n .

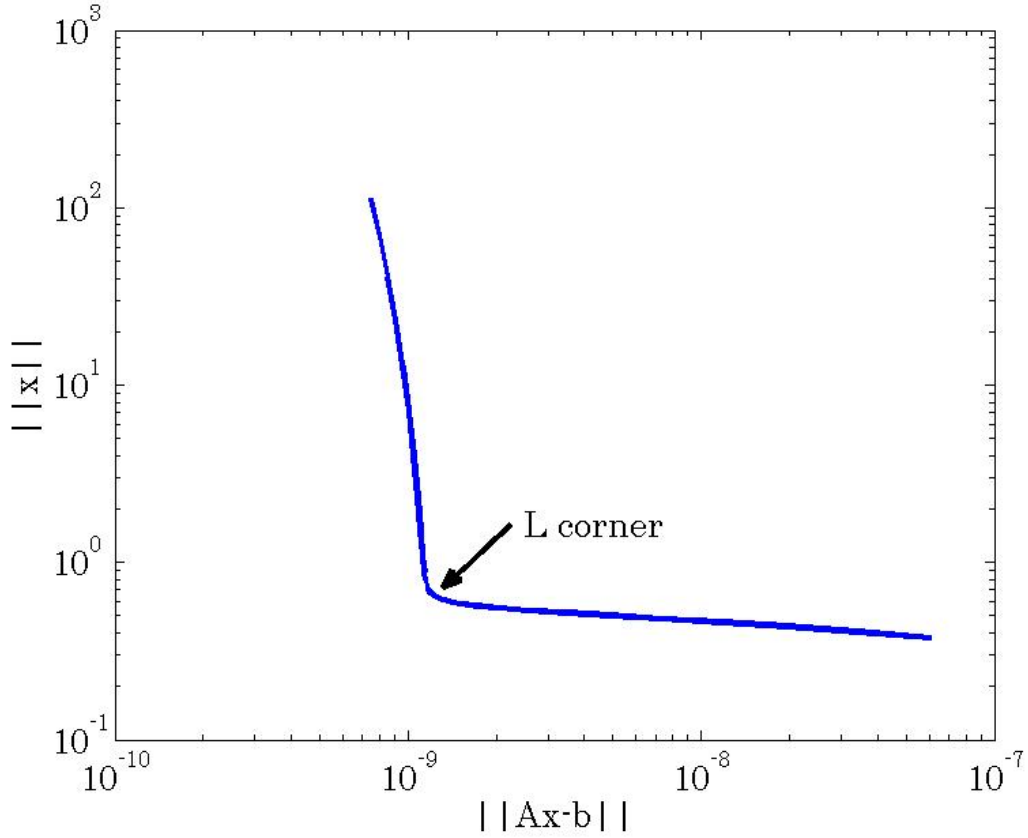


Figure 2.1. An example of the L curve.

In this thesis, the regularization parameter for both Tikhonov regularization in (1.4) and SIRA in (2.1) was selected by the L-curve method.

Moreover, unlike the case of Tikhonov regularization method, as given in (1.4), a batch solution does not exist. Nonetheless, there are several iterative methods proposed in the literatures, for example, the conjugate gradient descent method discussed in [52], the $l1_{ls}$ algorithm proposed in [48], and the split augmented Lagrangian shrinkage algorithm (SALSA) introduced in [1] etc. Among these algorithms, the SALSA algorithm is specifically designed for the ℓ_1 norm regularized image reconstruction problem.

The SALSA algorithm is an implementation of augmented Lagrangian method (ALM) or method of multipliers, where the unconstrained optimization problem in (2.1) is converted into an equivalent constrained problem

$$\min_{\mathbf{x}, \mathbf{v}} \{ \|\mathbf{Ax} - \mathbf{b}\|_2^2 + \lambda \|\mathbf{v}\|_1 \} \quad \text{subject to} \quad \mathbf{x} = \mathbf{v}. \quad (2.3)$$

By combining the constraint as a Lagrange multiplier to the minimization problem, (2.3) can be modified as

$$\min_{\mathbf{x}, \mathbf{v}} \{ \|\mathbf{Ax} - \mathbf{b}\|_2^2 + \lambda \|\mathbf{v}\|_1 + \frac{\mu}{2} \|\mathbf{x} - \mathbf{v}\|_2^2 \}, \quad (2.4)$$

where μ is the penalty parameter. Then the optimal solution of \mathbf{x} and \mathbf{v} can be solved iteratively. The reason of splitting variables in such a manner is (2.3) might be easier to solve than the original problem in (2.1).

Note that, due to the constraint in (2.3), the resulting cost function in (2.4) contains an ℓ_2 norm of the image coefficient, which can be considered as an additional regularization term. In case the cardinality of an image exceeds the average number of sources and detectors, correct reconstruction might still be able to obtain by increasing the parameter μ . Therefore, in this work, the SALSA algorithm was used to solve (2.1).

In order to demonstrate the advantages of this sparseness enhanced method as compared to the conventional Tikhonov regularization, a computer simulation was carried out. In the simulation, a CW DOT system was considered. The geometry of sources and detectors is illustrated in Fig. 2.2, where twenty five bifurcated optodes were placed as a 5×5 square grid over the top surface of a semi-infinite medium and centered at the origin. The distance between every two nearest optodes was 1.4 cm. The absorption and scattering coefficients of the homogeneous background medium

were chosen as $\mu_{a_0} = 0.06 \text{ cm}^{-1}$ and $\mu_{s_0} = 8.2 \text{ cm}^{-1}$, respectively. Two sphere like absorbers with identical absorption coefficients of $\mu_a = 0.46 \text{ cm}^{-1}$ and radii of 0.5 cm were placed along the y axis as shown in Fig. 2.3(a). Furthermore, since each optodes can be used as both light source and detector, by considering all the possible combination of optodes, 300 source-detector (S-D) pairs can be found. All the resulting S-D pairs were used for reconstruction. White Gaussian noise (WGN) was added to the relative measurement vector \mathbf{b} .

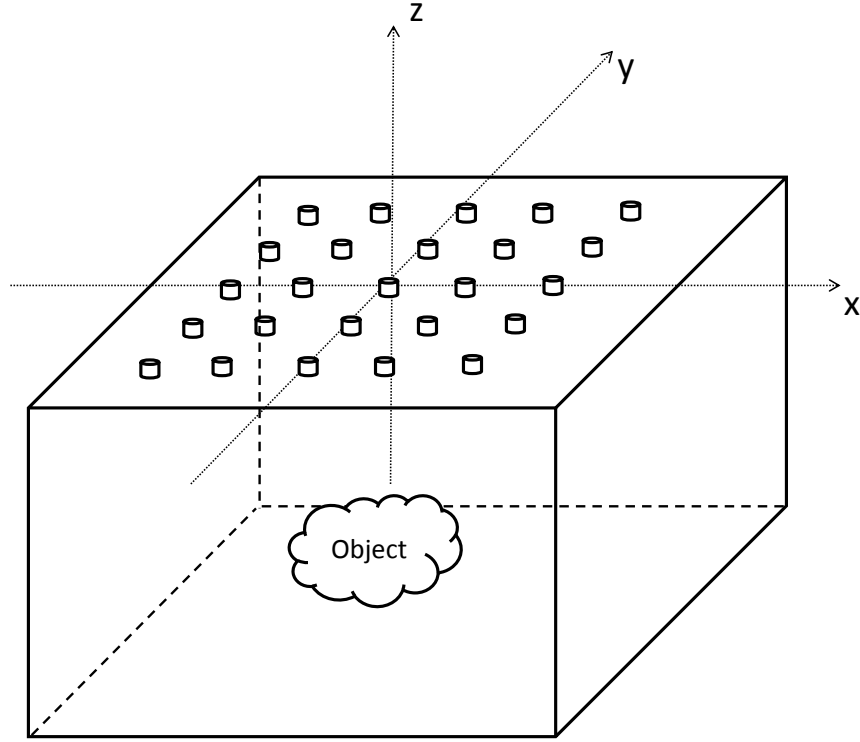


Figure 2.2. Geometry of the simulation and phantom experiments.

Figs. 2.3(b) and (c) are the reconstructed images using the Tikhonov method, as given in (1.4), and the SIRA, as given in (2.1). In order to emphasize the spatial

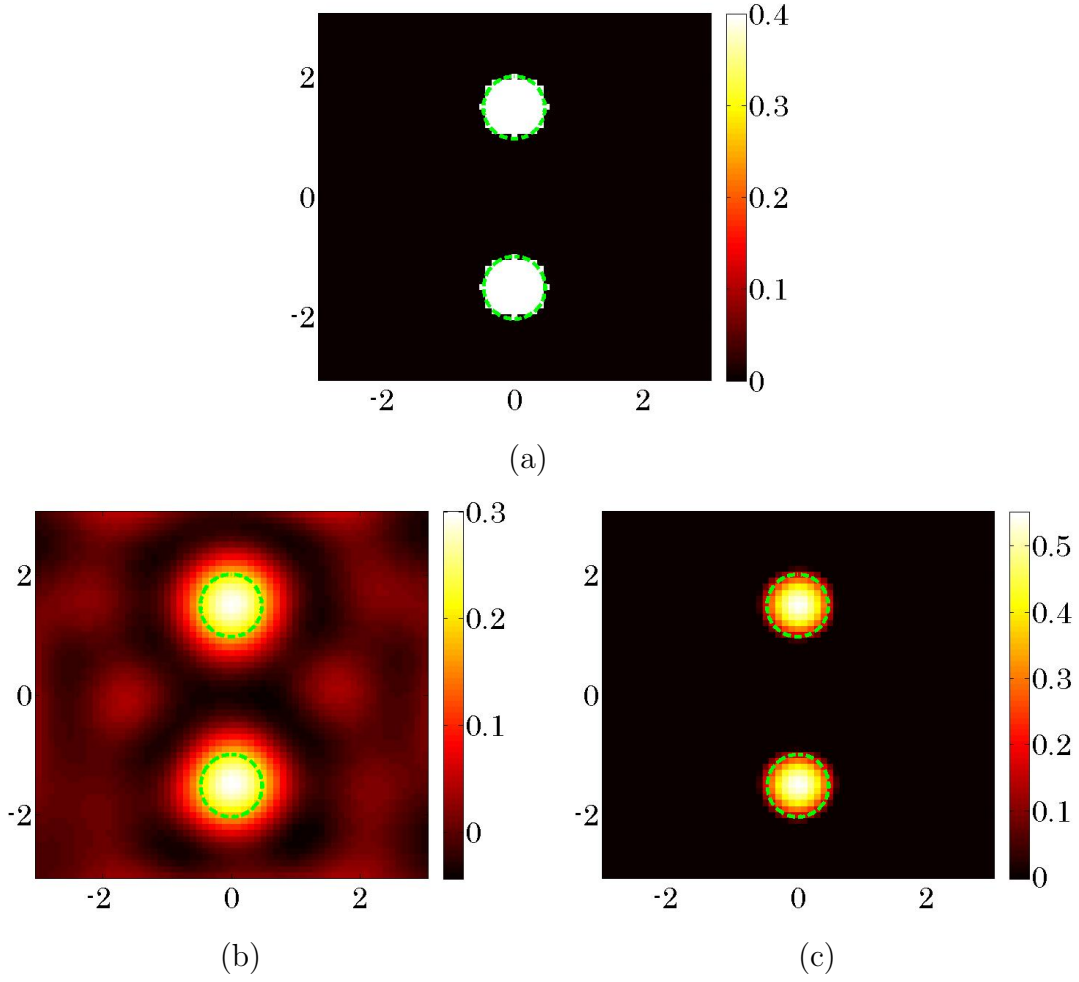


Figure 2.3. The original image (a) and the reconstructed images obtained using (b) Tikhonov method and (c) SIRA .

contrast, the reconstructed images were redisplayed in Fig. 2.4 using the log scale, i.e. $\log(|\hat{\mathbf{x}}|)$ was plotted. From the results in Figs. 2.3 and 2.4 one can clearly see that both methods identified the centers of the locations of the two objects correctly. However, it is evident that the sizes and sharpness of the imaged spheres were greatly improved by using the SIRA.

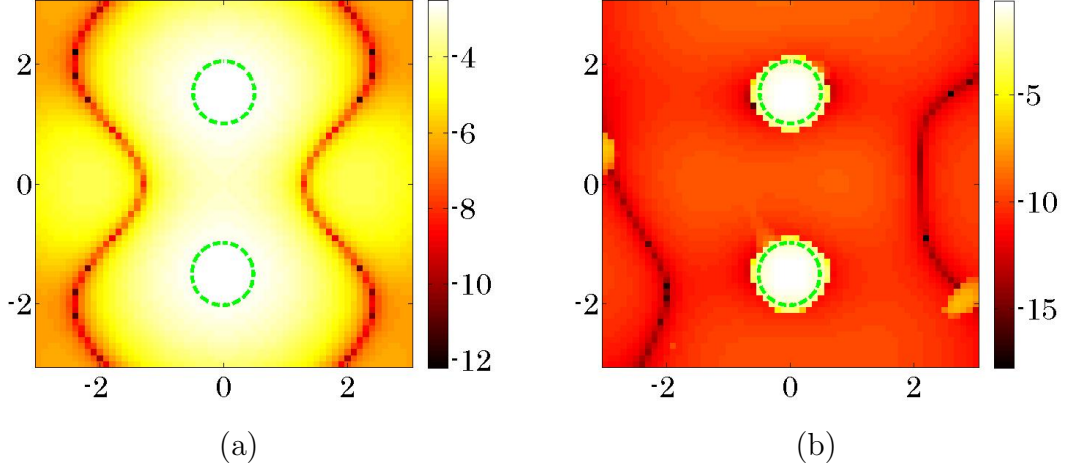


Figure 2.4. Reconstructed images obtained using (a) Tikhonov method and (b) SIRA in log scale .

2.2 The Depth of 3D DOT Reconstruction

In this section, the DOT image reconstruction problem is extended into the 3D scenario. With the same probe geometry designed as in the previous simulation, a spherical object with 0.5 cm radius was placed 2 cm below the S-D plane, as illustrated in Fig. 2.5. WGN was added to the relative measurements and the signal-to-noise ratio (SNR) was set to as 20 dB (i.e. the signal power was 100 times bigger than the noise power).

First the Tikhonov method as described in (1.4) was applied directly to reconstruct the image. The result is shown in Fig. 2.6(a). Compare to the original image, the object in the reconstruction is much larger than its original size, and the edge is blurry. Moreover, the center of the object is pulled toward the top surface. In other words, the reconstruction provided incorrect depth information. The SIRA algorithm in (2.1) was applied next and the result is shown in Fig. 2.6(b). Due to the sparsity regularization term, the size of the reconstructed object is almost identical to its actual one. However, its center position is still higher than its actual one.

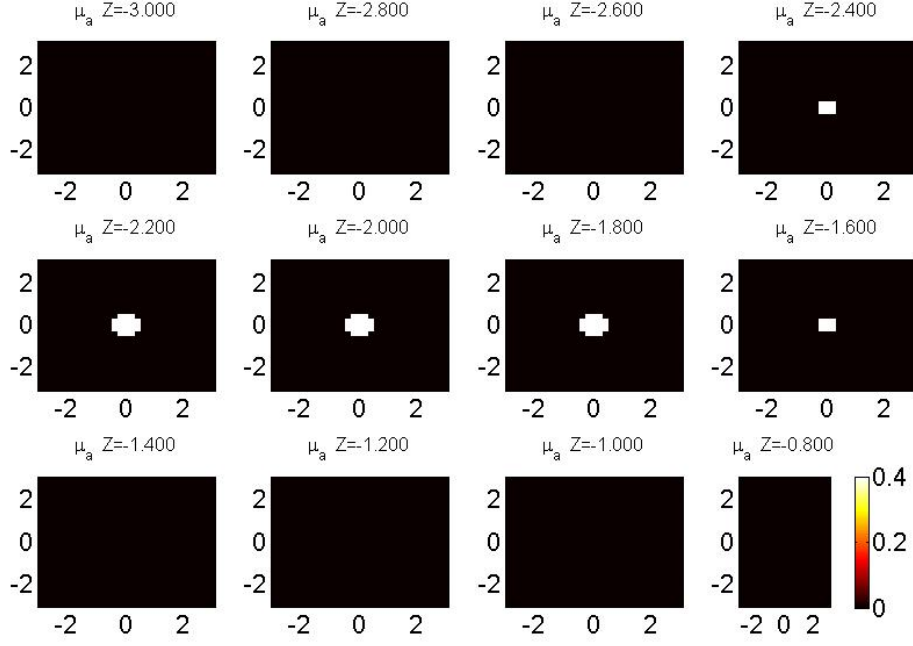
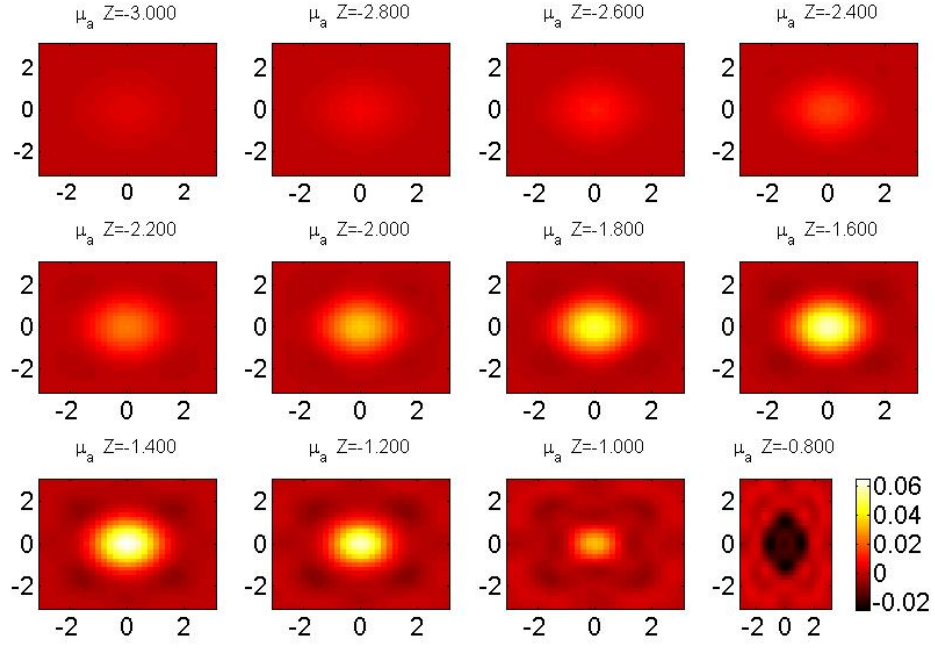
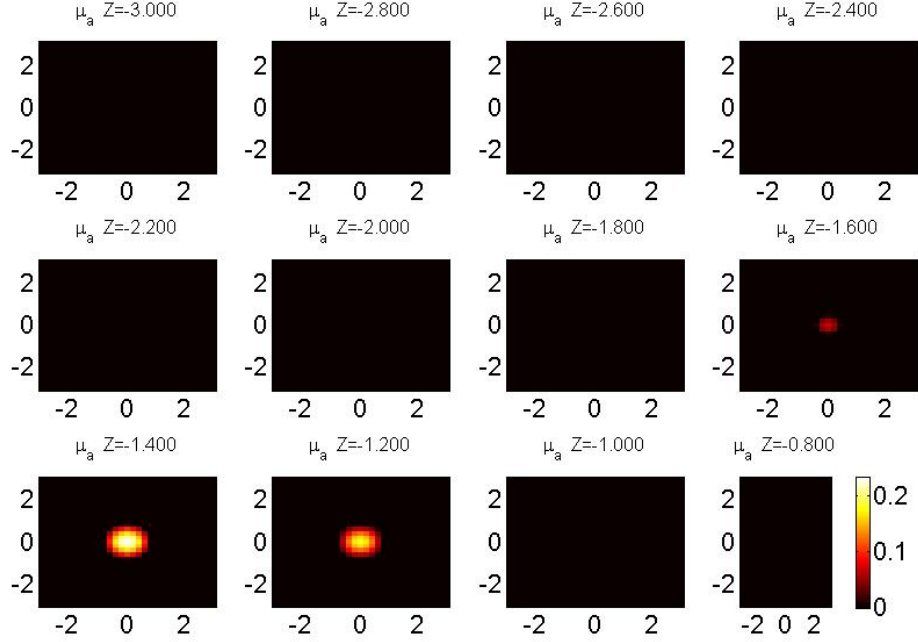


Figure 2.5. Original image for the 3D reconstruction simulation .

The depth problem of 3D DOT reconstruction was widely studied. A number of modified Tikhonov regularization algorithms were developed to fix the depth problem [31, 59, 71, 81]. The work in [71] was one of the methods that intended to fix the depth problem by using prior information obtained from other medical imaging modality such as ultrasound, x-ray, etc. It is suggested in [59, 81] that the reason behind the depth problem is the coefficients in the sensing matrix \mathbf{A} or the sensitivities of the incident lights drop exponentially when the corresponding voxel goes deeper. Fig. 2.7 illustrated the path of light when it propagated from one optode to the other. One can see that the photons are more likely to travel through the central area of the “banana” shape than its outer area, especially its lower portion. As a result, the lower portion of the medium is less sensitive in the measuring process due to this attenuation. Hence, methods that reweight the sensing matrix \mathbf{A} with respect to the corresponding depth



(a)



(b)

Figure 2.6. Reconstruction results of the 3D reconstruction simulations with (a) Tikhonov methods and (b) SIRA.

were reported accordingly. In [31] the regularization parameter in (1.4) is placed with a diagonal matrix \mathbf{D}_λ . Therefore, different regularization parameters can be assigned to different depth layers. Moreover, in [22] a normalization method was proposed where the Tikhonov method was modified as follows:

$$\hat{\mathbf{x}} = \arg \min_{\mathbf{x}} \{ \|\mathbf{Ax} - \mathbf{b}\|_2^2 + \lambda \|\mathbf{Lx}\|_2^2 \}. \quad (2.5)$$

The depth-dependent regularization matrix

$$\mathbf{L} = \sqrt{\text{diag}(\mathbf{A}^T \mathbf{A})},$$

in the regularization term of (2.5) can be considered as normalizing each column of the \mathbf{A} matrix by its ℓ_2 norm.

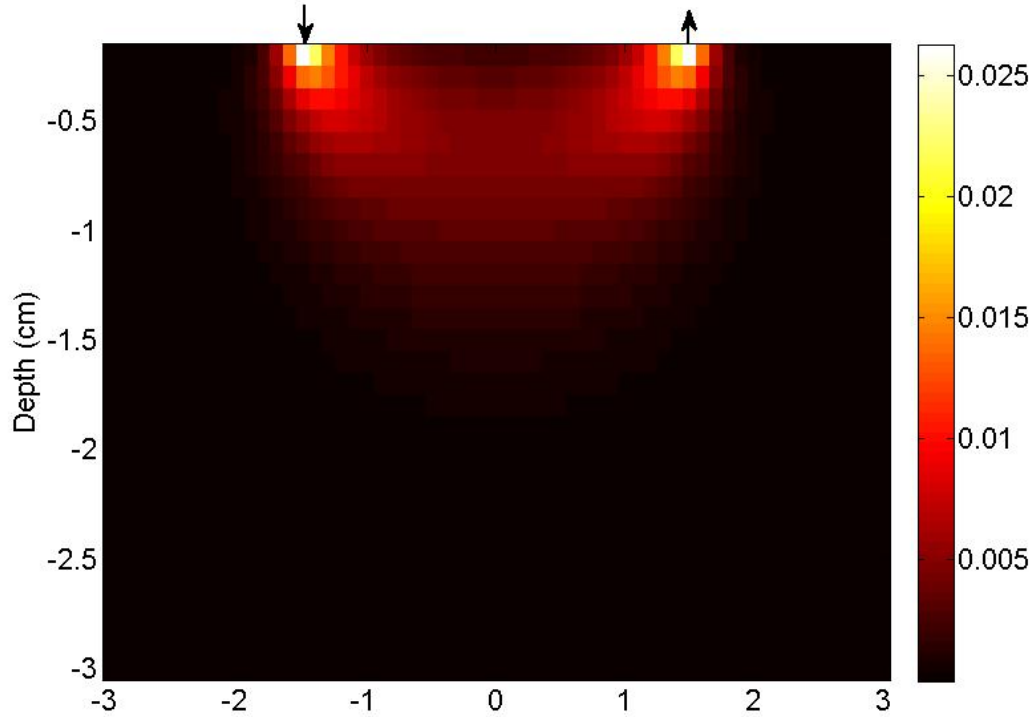


Figure 2.7. Measurement sensitivity when light propagates from one source to one detector.

Therefore, the key to fix the depth error in the 3D reconstruction is to combine the light attenuation information. A depth compensation algorithm (DCA) was proposed in [59] for the Tikhonov regularization method. Thereafter the ℓ_2 norm regularization term in [59] was replaced with a sparsity constraint, i.e. the ℓ_1 norm, as proposed in [45]. In the DCA method, the sensing matrix \mathbf{A} and the image coefficient vector \mathbf{x} in (1.3) are separated into multiple blocks with respect to their corresponding depths:

$$\begin{pmatrix} \mathbf{A}_1 & \mathbf{A}_2 & \cdots & \mathbf{A}_{nz} \end{pmatrix} \begin{pmatrix} \mathbf{x}_1 \\ \mathbf{x}_2 \\ \vdots \\ \mathbf{x}_{nz} \end{pmatrix} = \mathbf{b},$$

where nz is the number of layers along the depth direction. Then the largest eigenvalue or the ℓ_2 norm of each sub-matrix \mathbf{A}_i is calculated and represented as m_i . Then a diagonal matrix is defined as

$$D = \{diag[m_{nz}, m_{nz-1}, \cdots, m_2, m_1]\}^\gamma,$$

where γ is an adjustable parameter to adjust the depth of reconstructed objects. Consequently (2.1) can be modified into the following equation:

$$\hat{\mathbf{x}} = \arg \min_{\mathbf{x}} \{ \|\mathbf{A}^\# \mathbf{x} - \mathbf{b}\|_2^2 + \lambda \|\mathbf{x}\|_1 \}, \quad (2.6)$$

where the normalized sensing matrix $\mathbf{A}^\# = \mathbf{A}\mathbf{D}$.

Even though the DCA based approach has shown improvements in both spatial resolution and depth localization in the 3D DOT reconstruction, one clear disadvantage is that finding an appropriate tunable parameter γ is challenging. To avoid

this drawback, we modified the diagonal entries of the weighting matrix \mathbf{D} as the reciprocal of $\|A_i\|_2$ of each corresponding block:

$$D = [\frac{1}{m_1}, \frac{1}{m_2}, \dots, \frac{1}{m_{nz}}]. \quad (2.7)$$

This process can be considered as a light attenuation correction process. In next section, the developed method was tested by both computer simulation and laboratory phantom experiments.

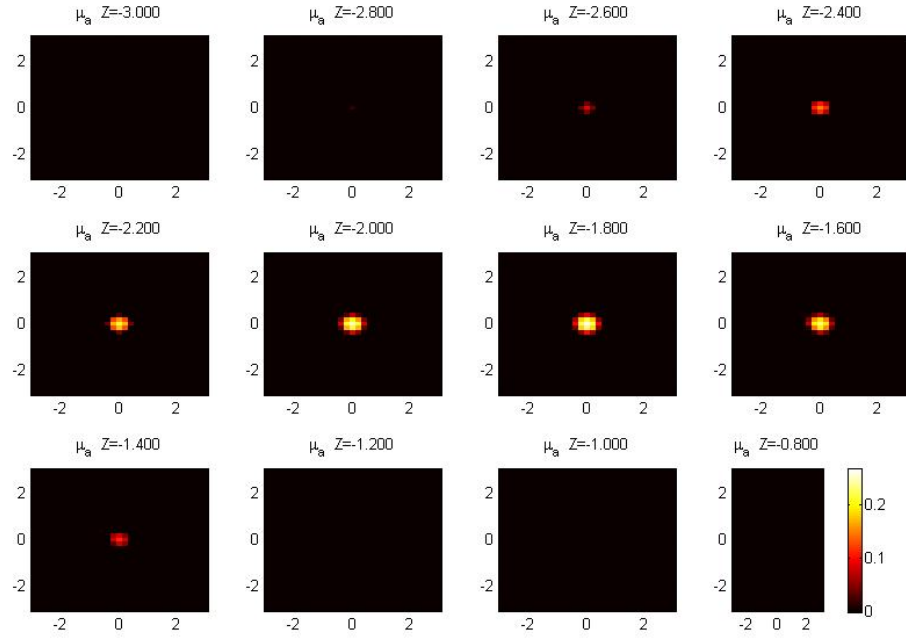
2.3 Experimental Results

2.3.1 Computer Simulation

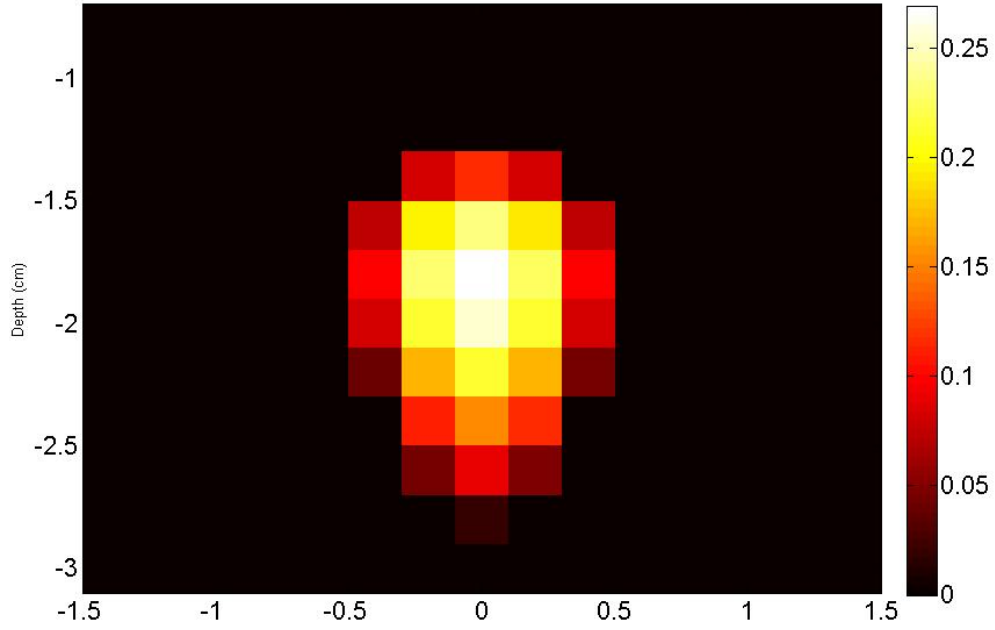
Applying (2.6) with the modified weighting matrix \mathbf{D} in (2.7) to reconstruct the previous simulation data, where a spherical object placed 2 cm below the S-D plane was measured. The reconstruction is shown in Fig. 2.8. Fig. 2.8(a) illustrates the reconstruction in the x - y plane of different depth layers. The spherical object can be found clearly in the center of the images for depths from -1.4 cm to -2.6 cm. In addition, a vertical slice at $y = 0$ is shown in Fig. 2.8(b). The reconstructed center of the object is approximately located at the depth of -1.8 cm, which was only one voxel (0.2 cm) above its actual depth (-2 cm). Despite the slight distortion along the depth direction, as compared to Fig. 2.6(b), the overall quality of the reconstructed image with the developed method has improved significantly.

2.3.2 Laboratory Experiment

A similar laboratory phantom experiment was also performed. A CW multi-channel NIR tomographic system (DYNOT, NIRx Medical Technologies) was used to take the measurements from a cubical container filled with 1% Intralipid solution, which has similar optical properties as normal human tissue. The geometry of the



(a)



(b)

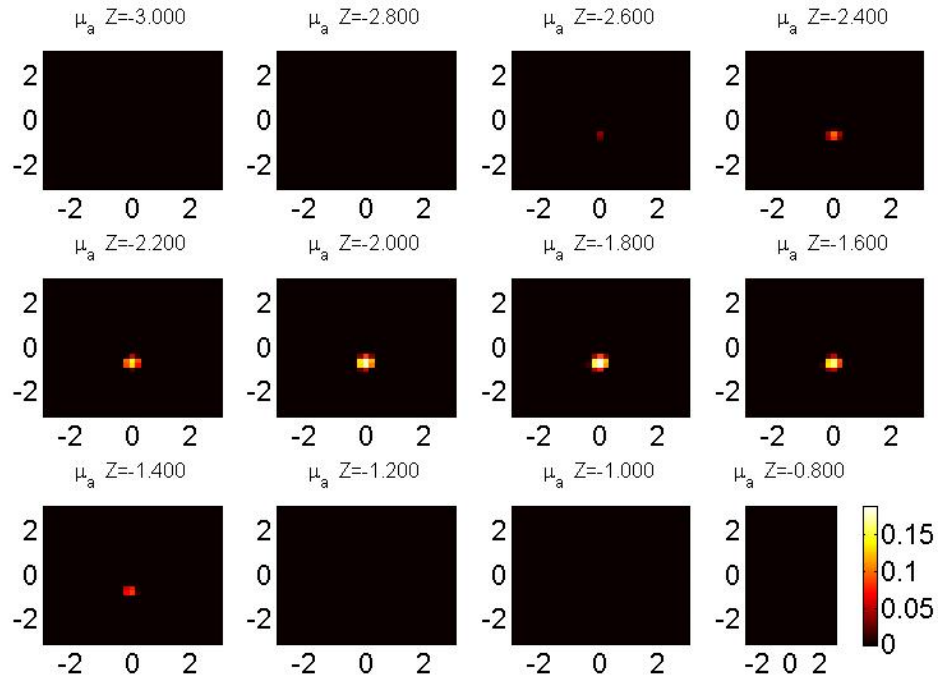
Figure 2.8. 3D Reconstruction of simulation data with a spherical object located at 2 cm below the S-D plane. (a) the x - y plane at different depth. (b) x - z plane when $y = 0$.

experiment was the same as that in the earlier computer simulation shown in Fig. 2.2. Twenty five bifurcated optodes were used with the distance between every two closest optodes 1.4 cm. Since each bifurcated optode can be used as both source and detector. By considering all the possible combination of different optodes, 300 measurement channels can be obtained. However, to eliminate the low SNR measurements, during the reconstruction process, only S-D pairs within 4.2 cm separation, which means up to the sixth nearest neighbors of each optode, were selected. As a result, 188 channels were used to collect measurements to maintain an acceptably high SNR. Moreover, a spherical absorber with a diameter of 1 cm is placed approximately 2 cm below the origin of the S-D plane.

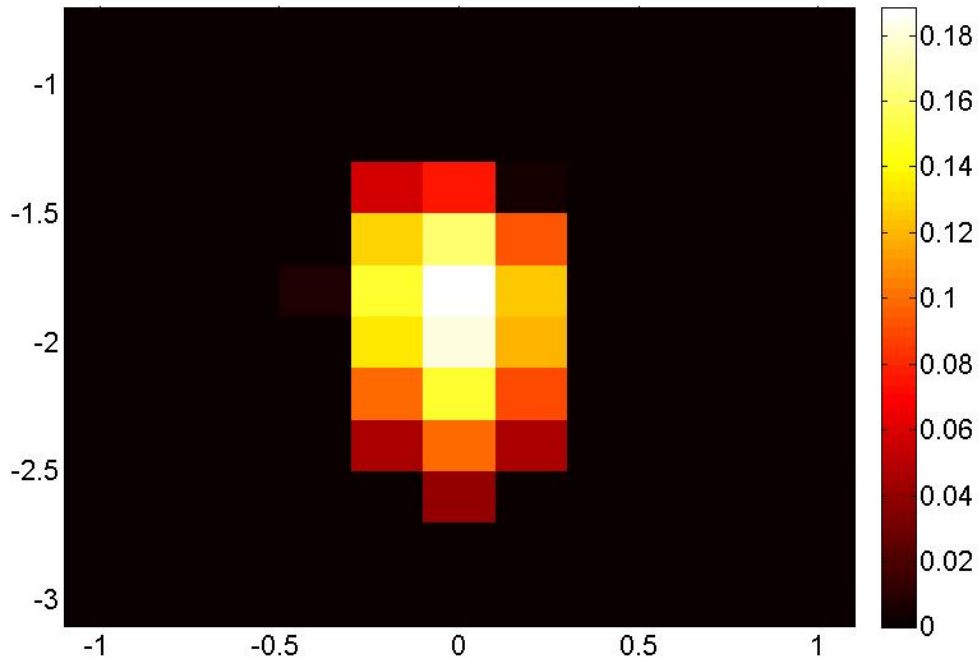
The reconstruction results are shown in Fig. 2.9. Similar to the simulation experiment, the images shown in Fig. 2.9(a) are slices along the x - y direction of different depth layers. A ball-shaped object can be found near the center of the slices corresponding to the depth from -1.4 cm to -2.6 cm. Due to the object was not located exactly in the origin, an x - z slice at $y = -0.6$ cm is shown in Fig. 2.9(b). The result is consist with the previous simulation experiment. As in both experiments, the reconstructed object is centered at the depth of -1.8 cm, which is slightly above its actual location.

2.4 Conclusion

In this chapter, an effective algorithm for 3D DOT reconstruction is discussed. This approach is based on the sparsity regularization and the attenuation correction of the measuring sensitivity. Such method manifested great improvement in the computer simulation as well as laboratory phantom experiment, where both the size and position of the object were recovered almost correctly. However, simply applying



(a)



(b)

Figure 2.9. 3D Reconstruction of phantom data with a spherical object located at 2 cm below the S-D plane. (a) the x - y plane at different depth. (b) x - z plane when $y = -0.6$.

such a sparsity regularized reconstruction method to a more practical clinical human experiment usually leads to poor results as explained in next chapter.

CHAPTER 3

IMPROVED RECONSTRUCTION WITH RELATIVE NOISE APPROXIMATION

In practice, measurement noise always exists, which can shield the true response signals and mislead to wrong conclusions when DOT is utilized to study in vivo brain activities stimulated under given tasks. In functional brain studies, the instrumental noise is usually inspected visually, where channels record significantly oscillating measurements or with low SNR are removed prior to physiological noise reduction process and image reconstruction steps [73, 47].

As in many of previous works, the noise added to \mathbf{b} is usually treated as white Gaussian noise (WGN) [14, 50, 26]. However, this might not be true in actual experimental measurements. Even though after the pre-selection process the remaining channels have relatively higher SNR than those removed ones, the noise level may still varied among different channels. Methods to design a weighting matrix for Tikhonov method were discussed in [36] and [79]. In [79], the so call generalized least-squares (GLS) method modified the Tikhonov method in (1.4) into

$$\hat{\mathbf{x}} = \arg \min_{\mathbf{x}} \{ \|\mathbf{D}\mathbf{A}\mathbf{x} - \mathbf{D}\mathbf{b}\|_2^2 + \lambda \|\mathbf{D}_x \mathbf{x}\|_2^2, \} \quad (3.1)$$

where \mathbf{D} and \mathbf{D}_x are diagonal matrices with the diagonal entries equal to the reciprocal of the corresponding standard deviation of noise and the pixel, respectively. With the appropriate noise variance information, the GLS method improves the reconstruction quality of conventional Tikhonov methods. The noise covariance matrix might be easy to obtain from both simulations and phantom experiments with fixed objects. Because in simulations the statistical information is known in advance, and in a static

phantom experiment, each measurement of individual S-D pairs can be modeled as constant, hence the noise variance of each S-D pair or channel can be found from a number of measurement samples. However, such a covariance matrix might be difficult to find for other applications where the measurements are dynamic or do not have enough samples available in order to estimate the covariance information, particularly for *in-vivo* brain imaging applications. Hence, an alternative noise quantification method is needed to weight the channels and consequently to promote the fidelity of the reconstructed images.

3.1 Approximation of The Relative Noise

Fig. 3.1 shows the noise variances seen at different channels with variable S-D separations of a laboratory phantom experiment. This clearly shows a larger variance as the S-D separation becomes bigger.

In this work, we introduced the sparse image reconstruction algorithm with noise normalization (SIRANN) by considering both the sparsity of the DOT images and the varying feature of noise variances. Eq.(2.1) is therefore modified by including a weight matrix \mathbf{D} , which normalizes the noise variances of the fidelity term [46, 79], as given below:

$$\hat{\mathbf{x}} = \arg \min_{\mathbf{x}} \{ \|\mathbf{D}\mathbf{A}\mathbf{x} - \mathbf{D}\mathbf{b}\|_2^2 + \lambda \|\mathbf{x}\|_1 \}, \quad (3.2)$$

where $\mathbf{D} = \text{diag}[1/\sigma_1, 1/\sigma_2, \dots, 1/\sigma_n]$, and σ_j^2 is the noise variance of the j -th channel, $1 \leq j \leq n$. One can also solve (3.2) by using the same algorithm as that used to solve (2.1) by setting $\mathbf{A}_D = \mathbf{D}\mathbf{A}$ and $\mathbf{b}_D = \mathbf{D}\mathbf{b}$.

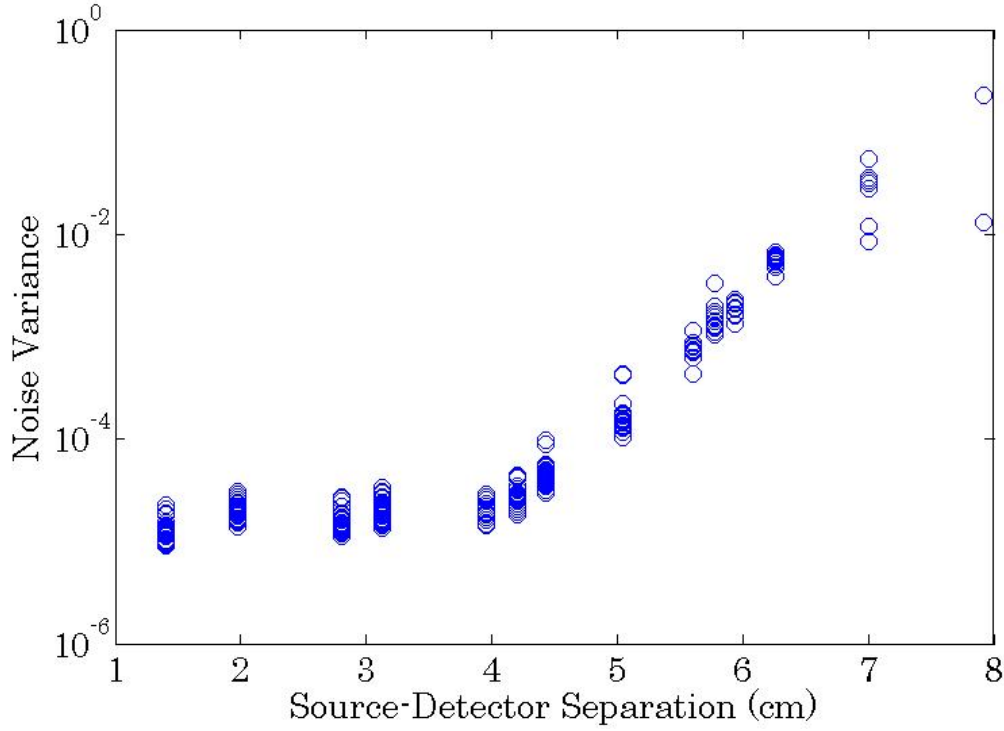


Figure 3.1. Noise variance of different S-D pairs in a laboratory phantom experiment.

3.1.1 Noise Analysis

In functional brain imaging by DOT, researchers often measure or determine changes in light intensity or photon density at different time instances. It follows that, with the linear Rytov approximation and modified Beer-Lambert law, the noise free relative signal changes measured by DOT, as expressed in (1.3), is given by

$$\mathbf{b} = \ln \frac{\Phi_0}{\Phi}, \quad (3.3)$$

where the baseline measurements or background measurement Φ_0 is the measured light or photon density at time instant t_1 , and Φ is the measured light density at a different time instant t_2 or activation measurement. Therefore, by considering the

measurement noise at these two time instants as \mathbf{w}_0 and \mathbf{w} , a noisy measurement is then given by

$$\begin{aligned}\tilde{\mathbf{b}} &= \ln \frac{\Phi_0 + \mathbf{w}_0}{\Phi + \mathbf{w}} \\ &= \ln \frac{\Phi_0}{\Phi} + \ln \frac{1 + \mathbf{w}_0/\Phi_0}{1 + \mathbf{w}/\Phi} \\ &= \mathbf{b} + \ln \frac{1 + \mathbf{w}_0/\Phi_0}{1 + \mathbf{w}/\Phi}.\end{aligned}\tag{3.4}$$

Hence, a noisy DOT measurement can be considered as the summation of a noise free relative light intensity measurement in (3.3) and the relative noise term \mathbf{z} , which is defined as:

$$\mathbf{z} = \ln \left(\frac{1 + \mathbf{w}_0/\Phi_0}{1 + \mathbf{w}/\Phi} \right).\tag{3.5}$$

Thus, the relative noise depends on both the original light intensity measurement, Φ_0 and Φ and the original noises, \mathbf{w}_0 and \mathbf{w} . Consequently, assuming the noise variances of different channels at different S-D separations are identical is not accurate or appropriate in this case.

As shown in [80], incorporating the noise variance information is a meaningful step to achieve high-quality DOT reconstructions. Before we start deriving a novel noise quantification method in the next section, we state the following assumptions that simplify the noise quantification process when the covariance matrix of (3.5) is approximated:

- (A1) Noise random variables of different S-D pairs are independent zero-mean Gaussian, namely, the covariance matrix $\mathbf{C}_{\mathbf{z}}$ is diagonal.
- (A2) The measurement noise variance is much less than the measured photon density or fluence, i.e., the SNR is high so that the probabilities of $\Pr(\mathbf{w}_0/\Phi_0 < -1)$ and $\Pr(\mathbf{w}/\Phi < -1)$ are almost zero.

The first assumption is acceptable if the noise from the sources is small and the detectors are taking the measurements from different locations independently. The second assumption is also valid since the noise amplitude of instrument is usually less than the measured signal amplitude; the system noise is usually assumed to be a few percent of the measured signals [83, 74].

3.1.2 Noise Variance Quantification

Eq. (3.5) can also be expressed as

$$\mathbf{z} = \ln \left(1 + \frac{\mathbf{w}_0}{\Phi_0} \right) - \ln \left(1 + \frac{\mathbf{w}}{\Phi} \right).$$

Now, based on the first assumption, the noise added to the i -th S-D channel is

$$z(i) = \ln \left(1 + \frac{w_0(i)}{\phi_0(i)} \right) - \ln \left(1 + \frac{w(i)}{\phi(i)} \right), \quad (3.6)$$

whose variance is equal to the i -th diagonal entry of the covariance matrix \mathbf{C}_w .

First, let $a = w_0(i)/\phi_0(i)$ and $b = w(i)/\phi(i)$, where $w_0(i)$ and $w(i)$ are Gaussian random variables with zero mean, and variances σ_1^2 and σ_2^2 , respectively. Then, because $\phi_0(i)$ and $\phi(i)$ are constants, a and b are also zero mean Gaussian random variables with variances $\sigma_a^2 = \sigma_1^2/\phi_0^2(i)$ and $\sigma_b^2 = \sigma_2^2/\phi^2(i)$, respectively.

Furthermore, due to Assumption (A2), the variance of both a and b should be much less than 1. Therefore, (3.6) becomes

$$z(i) = \ln(1 + a) - \ln(1 + b),$$

whose variance is

$$\begin{aligned}
\sigma_{z(i)}^2 &= E[z^2(i)] - (E[z(i)])^2 \\
&= E[(\ln(1+a) - \ln(1+b))^2] - (E[\ln(1+a) - \ln(1+b)])^2 \\
&= E[(\ln^2(1+a))] + E[(\ln^2(1+b))] \\
&\quad - (E[\ln(1+a)])^2 - (E[\ln(1+b)])^2 \\
&= \text{Var}[\ln(1+a)] + \text{Var}[\ln(1+b)].
\end{aligned}$$

Since both a and b are Gaussian with small variance, let

$$g(x) = \ln(1+x), \quad (3.7)$$

where x is normal, i.e., $x \sim N(0, \sigma_x^2)$ with $\sigma_x \ll 1$.

Applying Taylor expansion to (3.7) yields:

$$g(x) = \sum_{k=1}^{\infty} (-1)^{k+1} \frac{x^k}{k},$$

for $-1 < x < 1$. Hence,

$$E[g(x)] = \sum_{k=1}^{\infty} (-1)^{k+1} \frac{E[x^k]}{k}.$$

By using the fact that the odd moments of Gaussian distribution are zero,

$$\begin{aligned}
E[g(x)] &= \sum_{k \text{ is even}} \frac{(-1)^{k+1}}{k} \sigma_x^k (k-1)!! \\
&= - \sum_{k=1}^{\infty} \frac{(2k-1)!!}{2k} \sigma_x^{2k}, \quad (3.8)
\end{aligned}$$

where $k!!$ is the double factorial, defined by $k!! = k(k-2) \cdots 5 \cdot 3 \cdot 1$ if k is a positive odd number [3].

Similarly,

$$\begin{aligned}
E[g^2(x)] &= E \left[\left(\sum_{i=1}^{\infty} (-1)^{i+1} \frac{x^i}{i} \right) \left(\sum_{j=1}^{\infty} (-1)^{j+1} \frac{x^j}{j} \right) \right] \\
&= \sum_{i=1}^{\infty} \sum_{j=1}^{\infty} \frac{(-1)^{i+j}}{ij} E[x^{i+j}] \\
&= \sum_i \sum_j \frac{(i+j-1)!!}{ij} \sigma_x^{i+j}, \tag{3.9}
\end{aligned}$$

where $i + j$ is even.

Since the variance of x is much less than one, (3.8) can be approximated as:

$$E[g(x)] \approx - \left(\frac{1}{2} \sigma_x^2 + \frac{3}{4} \sigma_x^4 + \frac{5}{2} \sigma_x^6 + O(\sigma_x^8) \right)$$

Hence,

$$\begin{aligned}
E^2[g(x)] &\approx \left(\frac{1}{2} \sigma_x^2 + \frac{3}{4} \sigma_x^4 + \frac{5}{2} \sigma_x^6 + O(\sigma_x^8) \right)^2 \\
&\approx \frac{1}{4} \sigma_x^4 + \frac{3}{4} \sigma_x^6 + O(\sigma_x^8)
\end{aligned}$$

Similarly, (3.9) can be approximated as:

$$E[g^2(x)] \approx \sigma_x^2 + \frac{11}{4} \sigma_x^4 + \frac{137}{12} \sigma_x^6 + O(\sigma_x^8).$$

Therefore, the variance of $g(x)$ can be found from the following equation:

$$\begin{aligned}
\text{Var}(g(x)) &= E[g^2(x)] - E^2[g(x)] \\
&\approx \sigma_x^2 + \frac{5}{2} \sigma_x^4 + \frac{32}{3} \sigma_x^6 + O(\sigma_x^8).
\end{aligned}$$

Followed by these results, we have:

$$\begin{aligned}
E[z(i)] &= E[\ln(1 + w_0(i)/\phi_0(i))] - E[\ln(1 + w(i)/\phi(i))] \\
&\approx -\left(\frac{1}{2} \left(\frac{\sigma_1^2(i)}{\phi_0^2(i)} - \frac{\sigma_2^2(i)}{\phi^2(i)}\right) + \frac{3}{4} \left(\frac{\sigma_1^4(i)}{\phi_0^4(i)} - \frac{\sigma_2^4(i)}{\phi^4(i)}\right) \right. \\
&\quad \left. + \frac{5}{2} \left(\frac{\sigma_1^6(i)}{\phi_0^6(i)} - \frac{\sigma_2^6(i)}{\phi^6(i)}\right) + O(\sigma^8)\right) \\
&\approx 0
\end{aligned}$$

$$\begin{aligned}
\sigma_{z(i)}^2 &= \text{Var}[\ln(1 + w_0(i)/\phi_0(i))] + \text{Var}[\ln(1 + w(i)/\phi(i))] \\
&\approx \left(\frac{\sigma_1^2(i)}{\phi_0^2(i)} + \frac{\sigma_2^2(i)}{\phi^2(i)}\right) + \frac{5}{2} \left(\frac{\sigma_1^4(i)}{\phi_0^4(i)} + \frac{\sigma_2^4(i)}{\phi^4(i)}\right) \\
&\quad + \frac{32}{3} \left(\frac{\sigma_1^6(i)}{\phi_0^6(i)} + \frac{\sigma_2^6(i)}{\phi^6(i)}\right) + O(\sigma^8)
\end{aligned} \tag{3.10}$$

Hence the variance of the relative noise of one S-D channel can be obtained from the above equation consisting of original noise variances and the amplitude of the original measurements at different time instances.

Note that even if the original noise terms \mathbf{w}_0 and \mathbf{w} are WGN, due to the Φ_0 and Φ terms, the noise variances of (3.5) as derived in (3.10) are no longer the same among different channels.

3.1.3 Numerical Validation

In order to verify the noise quantification method just derived above, two sets of data were collected from a phantom experiment: Φ_0 readings were related to the base line measurements from all the S-D channels, which were taken when the absorbers were removed from the medium; corresponding Φ values were acquired from the measurements with the objects inside the medium. Both Φ_0 and Φ were taken with 100 sampling points, separately. The mean and the variance of Φ_0 and Φ over 100

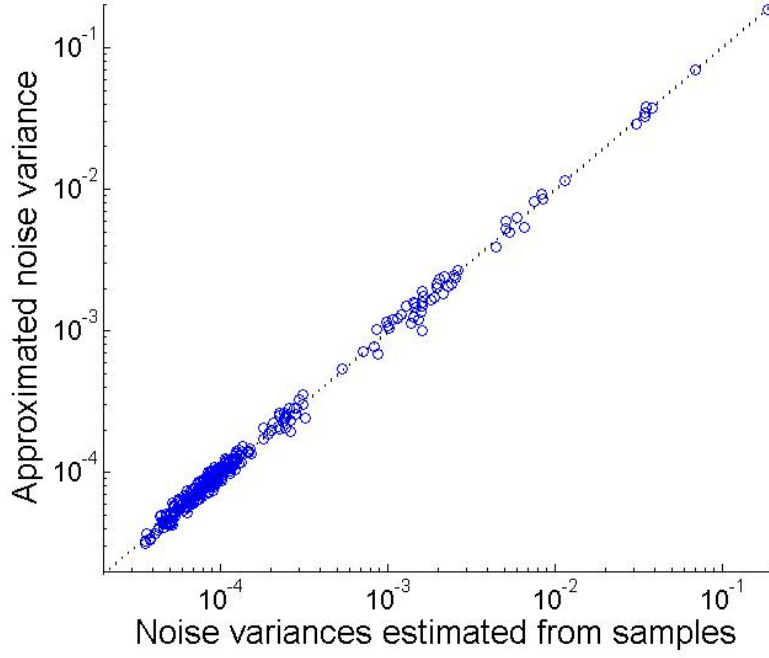


Figure 3.2. Comparison between the actual noise variance and the estimated noise variance.

samples were computed and used to calculate the relative noise variance with (3.10). A comparison between the approximated noise variance by the noise quantification method in (3.10) with the actual one estimated from the 100 samples is given in Fig. 3.2. The approximated noise variances quantified by (3.10) are consistent with the actual ones. The mean square error between the estimated and actual noise variance was calculated as 1.7609×10^{-9}

3.1.4 Noise Quantification Assisted DOT Image Inversion

Note that in (3.5), the measurement noise \mathbf{w}_0 and \mathbf{w} are actually the noise from the same S-D channels at different time instances. By further assuming that the noise does not change over time, i.e. $\sigma_a^2 = \sigma_b^2 = \sigma_z^2$, (3.10) can be modified as

$$\begin{aligned} \sigma_{z(i)}^2 \approx & \sigma_z^2 \left(\frac{1}{\phi_0^2(i)} + \frac{1}{\phi^2(i)} \right) + \frac{5}{2} \sigma_z^4 \left(\frac{1}{\phi_0^4(i)} + \frac{1}{\phi^4(i)} \right) \\ & + \frac{32}{3} \sigma_z^6 \left(\frac{1}{\phi_0^6(i)} + \frac{1}{\phi^6(i)} \right) + O(\sigma_z^8). \end{aligned} \quad (3.11)$$

This simplification also makes the noise quantification method more practical and suitable for most of DOT applications. In practice, the noise variance of each S-D channel, σ_z^2 , can be easily measured in advance (e.g. it can be estimated using a short acquisition from the baseline measurement). Then with (3.11), the noise variances of the relative measurements can be easily calculated. The weighting matrix \mathbf{D} in (3.2) now becomes:

$$\mathbf{D} = \begin{pmatrix} \frac{1}{\sigma_{z(1)}} & & & \\ & \frac{1}{\sigma_{z(2)}} & & \\ & & \ddots & \\ & & & \frac{1}{\sigma_{z(n)}} \end{pmatrix}.$$

One can notice that the estimated variances of the relative noise can be considered as the noise power to signal power ratio of one channel. Hence its reciprocal or the weighting coefficient relates to the SNR of each channel. As a result, measurements from high SNR channels gain higher weights as compared to those with a low SNR, as implied in the weighting matrix \mathbf{D} .

It should also be noted that for the applications that the original noise level cannot be estimated, one can simply assume that the noise variances among different channels are identical (i.e., $\sigma_a = \sigma_b = 1$) for all the channels. Then, the measured

amplitudes can be used to estimate the relative noise variances and to build the weight matrix.

3.2 Experimental Results

The derived noise quantification method along with the SIRANN algorithm is tested by computer simulation, laboratory phantom, and the Human finger tapping experiments.

3.2.1 Computer Simulation

A computer simulation was first implemented. In the simulation, a continuous wave (CW) DOT system was considered. The geometry of sources and detectors was the same as previous experiments in Ch. 2, which is illustrated in Fig. 2.2, where twenty five bifurcated optodes were placed as a 5×5 square grid over the top surface of a semi-infinite medium and centered at the origin. The distance between every two closest optodes was 1.4 cm. By using the first to sixth nearest S-D pairs or S-D pairs within 4.2 cm separation, 188 channels can be obtained. White Gaussian noise was added to both background measurements Φ_0 and inhomogeneous measurements Φ .

The absorption and reduced scattering coefficients of the homogeneous background medium were chosen in a reasonable range [16] as $\mu_{a0} = 0.06 \text{ cm}^{-1}$ and $\mu_{s0} = 8.2 \text{ cm}^{-1}$, respectively. The forward model was computed analytically as in [59]. Since the main focus of this study is to improve the spatial resolution for functional brain imaging, where only relative changes in absorption within activated brain areas are considered. Thus, the difference in absorption, $\Delta\mu_a$, between the imaged brain area and background is what we need to reconstruct for DOT images. An “L” shape absorber with $\Delta\mu_a = 0.1 \text{ cm}^{-1}$ was placed in the center of a relative zero background as shown in Fig. 3.3, at a depth of 1.5 cm.

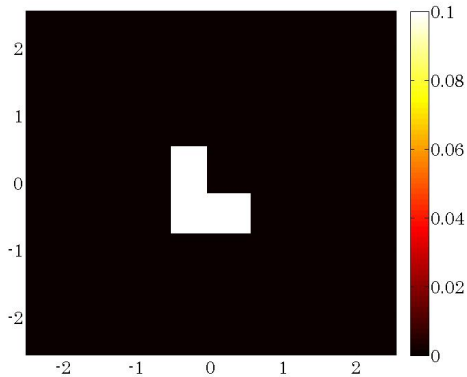


Figure 3.3. The original image used for the simulation.

In order to demonstrate the advantage of the SIRANN method with our new noise quantification method, we compared the reconstruction results with the conventional Tikhonov regularization method in (1.4), the GLS method in (3.1), and with SIRA in (2.1). The regularization parameters in Tikhonov regularization methods were selected with the L-curve approach[77], as it is effective to provide the optimal solution and thus commonly used with Tikhonov regularization methods. For all the other methods, the regularization parameter were selected from a number of trails that yielded the least distortion of the imaged object’s shape. Moreover, methods besides Tikhonov regularization were all performed by the SALSA algorithm [1], a solver for convex optimization problems, with the same stopping criteria.

The results are shown in Fig. 3.4(a)-(d). The result by Tikhonov regularization method, shown in Fig. 3.4(a), is blurry; the shape of the object is completely distorted from the “L” shape into an elliptical object. With the noise normalization, the GLS method improved the shape of the reconstructed object as compared to the Tikhonov method. However, the recovered object is still fuzzy and with background noise. The SIRA is giving a less blurred image shown in Fig. 3.4(c), but the shape of the object tends to be a “C” shape, which is still incorrect. At the end, the reconstruction

with the noise quantification assisted SIRANN method gives rise to very consistent reconstructed image that recovers the original image almost completely, as shown in Fig. 3.4(d).

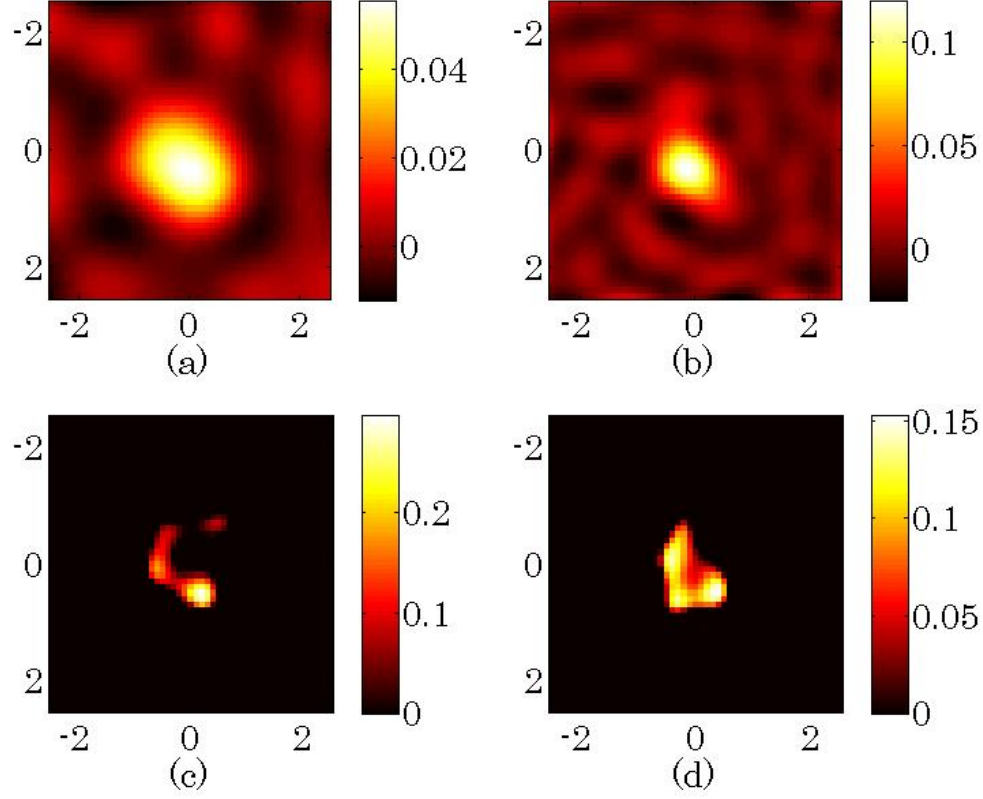


Figure 3.4. Comparison of the reconstructions with:(a)Tikhonov (b) GLS; (c) SIRA; (d) SIRANN.

To show the improvement of proposed noise quantification method, two quantitative metrics were also computed: the structural similarity index metric (SSIM)[78] and the contrast-to-noise ratio (CNR) [69].

The SSIM is given by

$$\text{SSIM}(\mathbf{x}, \mathbf{y}) = \left(\frac{2\mu_{\mathbf{x}}\mu_{\mathbf{y}}}{\mu_{\mathbf{x}}^2 + \mu_{\mathbf{y}}^2} \right) \left(\frac{2\sigma_{\mathbf{xy}}}{\sigma_{\mathbf{x}}^2 + \sigma_{\mathbf{y}}^2} \right),$$

38

where $\mu_{\mathbf{x}}, \mu_{\mathbf{y}}, \sigma_{\mathbf{x}}^2, \sigma_{\mathbf{y}}^2$ are the means and variances of vector \mathbf{x} and \mathbf{y} , respectively. $\sigma_{\mathbf{xy}}$ is the covariance between vector \mathbf{x} and \mathbf{y} .

On the other hand, by defining the region of interest (ROI) as the area of targeting object and the rest as background (BKG), the CNR is calculated by:

$$\text{CNR} = \frac{\overline{\mu_{ROI}} - \overline{\mu_{BKG}}}{\sqrt{c_1 \sigma_{\mu_{ROI}}^2 + c_2 \sigma_{\mu_{BKG}}^2}},$$

where $\overline{\mu_{ROI}}$ and $\overline{\mu_{BKG}}$ are the average coefficients of ROI and BKG, $\sigma_{\mu_{ROI}}^2$ and $\sigma_{\mu_{BKG}}^2$ are the variances of the coefficients of the two, and c_1 and c_2 are the weighting coefficients that are calculated from

$$c_i = \frac{\text{Number of pixels in ROI/BKG}}{\text{Total number of pixels in the image}}, \quad i = 1, 2.$$

The SSIM and the CNR of all these four methods were computed and listed in Table. 3.1. Notice that the SSIM from the SIRANN method was the highest among all the methods we have tested, meaning that because of the sparse image reconstruction algorithm and the noise normalization process, the structural of the object in the reconstructed image was very close to the actual one.

Table 3.1. SSIM and CNR values of simulation reconstructions with Tikhonov, GLS, SIRA, and SIRANN.

Method	SSIM	CNR
Tikhonov	0.60	4.56
GLS	0.76	6.11
SIRA	0.61	4.08
SIRANN	0.92	11.97

The high CNR indicates that most of the non-zero pixels are located in the ROI. Even though SIRA method yielded clean background, its CNR is the lowest.

This is due to the distortion, some of the non-zero pixels were fallen outside the ROI and therefore been considered as background noise in the CNR calculation. On the other hand, the proposed method recovered the object almost completely with a clean background, therefore its CNR value is the highest among all the methods tested in the experiment.

3.2.2 Laboratory Experiment

Next, a laboratory phantom experiment was performed to test our newly derived reconstruction method with real experimental noise. In the phantom experiment, the experimental setup and procedures were similar to those used in [59]: A CW-based DOT imaging system (DYNOT, NIRx, New York) was used to obtain the measurements from a container of $15 \times 10 \times 10 \text{ cm}^3$ filled with 1% Intralipid solution. The optodes were placed on the very top surface of the intralipid solution such that the tips of optodes were just touching the liquid phantom surface. In this way, no air gap existed between the tips and liquid to minimize the refractive index (RI) mismatch. This setup provided us with a very similar boundary condition to that in light-tissue interaction situation. Thus, our experimental setup did not deviate too much from the traditional light-tissue interaction setup. The wavelength of incident light was 830 nm. The absorption and reduced scattering coefficients of the homogeneous background medium were measured with a frequency domain system (Model 96208, ISS Inc., Champaign, Illinois) at the same 830nm wavelength as $\mu_{a_0} = 0.12 \text{ cm}^{-1}$ and $\mu_{s_0} = 8.8 \text{ cm}^{-1}$, respectively. The geometry of sources and detectors is the same as computer simulation as illustrated in Fig. 2.2, where twenty five bifurcated optodes were placed as a 5×5 square grid over the top surface of the Intralipid medium and centered at the origin. By considering all the possible combination of different optodes, 300 measurement channels can be obtained and the SNRs of

all these channels were calculated as shown in Fig.3.5. It can be noticed that the SNRs of the first to the sixth nearest S-D pairs were relatively higher than the rest separations. Therefore, to avoid channels with significantly low SNR level, only first to sixth nearest S-D pairs were selected. As a result, 188 channels were used to collect measurements. Two spherical absorbers with identical sizes (diameter = 1 cm), were placed along the y axis, 1.5 cm below the measurement surface. The center to center distance between the two absorbers was 1.5 cm.

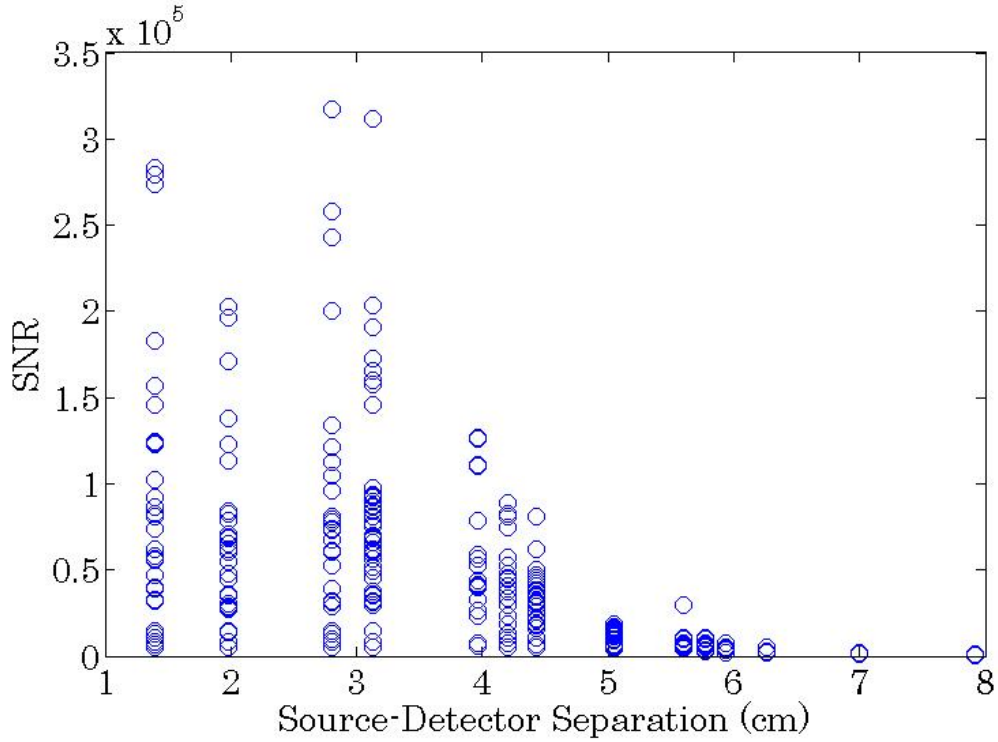


Figure 3.5. Calculated SNRs among different channels in the phantom experiment.

Moreover, strong light scattering of biological tissue causes the detection sensitivity of DOT to attenuate exponentially with increased depth, resulting in depth localization in DOT to be poor in general. Thus, it becomes unrealistic to accurately quantify the local absorption perturbation without knowing its actual depth. A va-

riety of efforts have been made by different research groups to improve the accuracy in depth localization. One common method that is currently used in functional brain imaging was introduced by combining DOT with prior anatomical information from MRI, assuming that all the optical signals come from a fixed depth or layer below the measurement surface [10]. This is specifically realized by the utilization with a cortical constraint (resulting from spatial prior information from structural and functional MRI) to reduce DOT partial volume error and to improve quantitative accuracy for reconstructed DOT images. This means that in DOT reconstruction, a 2D image is reconstructed at a pre-selected depth. In this way, a 3D reconstruction problem is reduced to a 2D slice reconstruction problem. This is how we obtain 2D reconstructed images from our 3D experimental space.

Figure. 3.6 shows the reconstructed images using the Tikhonov method, as given in (1.4), with the regularization parameter selected by the L-curve method[41]: $\lambda = 10^{-4}$, the SIRA, as given in (2.1), with $\lambda = 3 \times 10^{-4}$, and the SIRANN algorithm with proposed noise quantification method, and regularization parameter $\lambda = 3 \times 10^{-5}$. Despite the slight distortion of one absorber, reconstruction result by using SIRA successfully shows two objects along the vertical axis, while Tikhonov method failed to recover the structure of two absorbers inside the medium. It is clear that the sparsity enhanced method indeed improved the spatial resolution of the reconstructed image. However, due to the measurement noise, the lower object in the image tended to be smaller than its actual size. On the other hand, thanks to the appropriate noise whitening process, the lower object in the reconstructed image of our proposed method ,as shown in Fig. 3.6(c), was showing a comparable size to the actual one with smaller distortion of the shape. In order to emphasize the spatial contrast, the cross sections of all the results from Tikhonov, SIRA, and the proposed method at

$x=0$ (i.e., along y -axis) are also plotted in Fig. 3.7. As one can see, two objects were better separated with the proposed method.

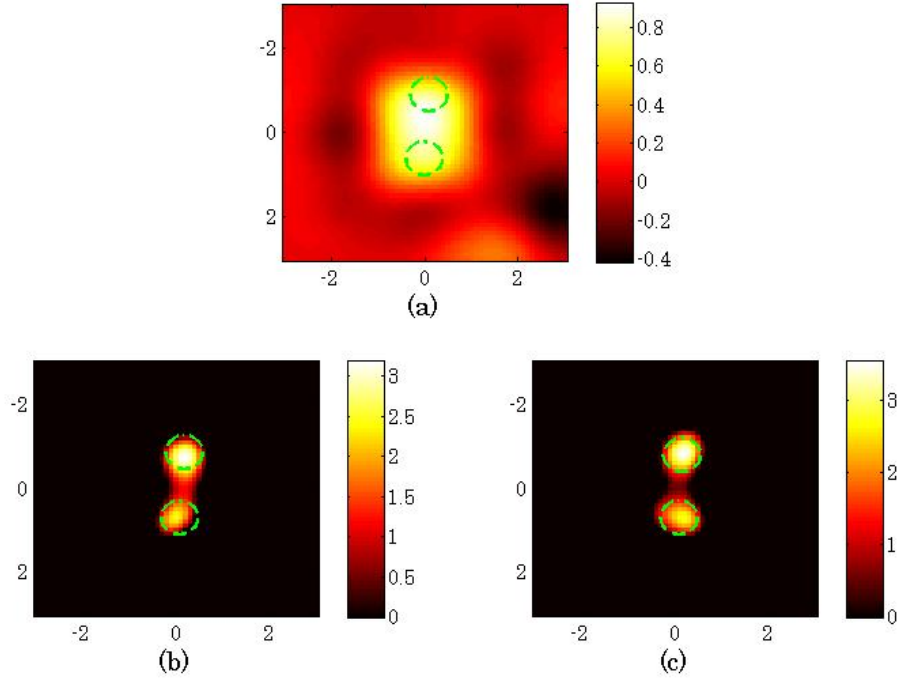


Figure 3.6. Reconstructed images obtained by using (a) Tikhonov method, (b) SIRA, and (c) SIRANN with derived noise quantification method.

For the sake of better illustrating the advantage of our proposed method, another phantom experiment was implemented. In the second experiment, the two spherical absorbers used in the previous experiment were replaced by an “L” shape object as shown in Fig. 3.8, where the grid on the background is $5 \text{ mm} \times 5 \text{ mm}$.

In Fig. 3.9, we compared the reconstruction results from Tikhonov method, GLS method, SIRA, and the proposed noise quantification assisted SIRANN method, with the regularization parameter $\lambda = 10^{-5}, 8 \times 10^{-7}, 2 \times 10^{-5}$, and 8×10^{-6} , respectively. Though all of the four methods recovered an absorber in the center of images,

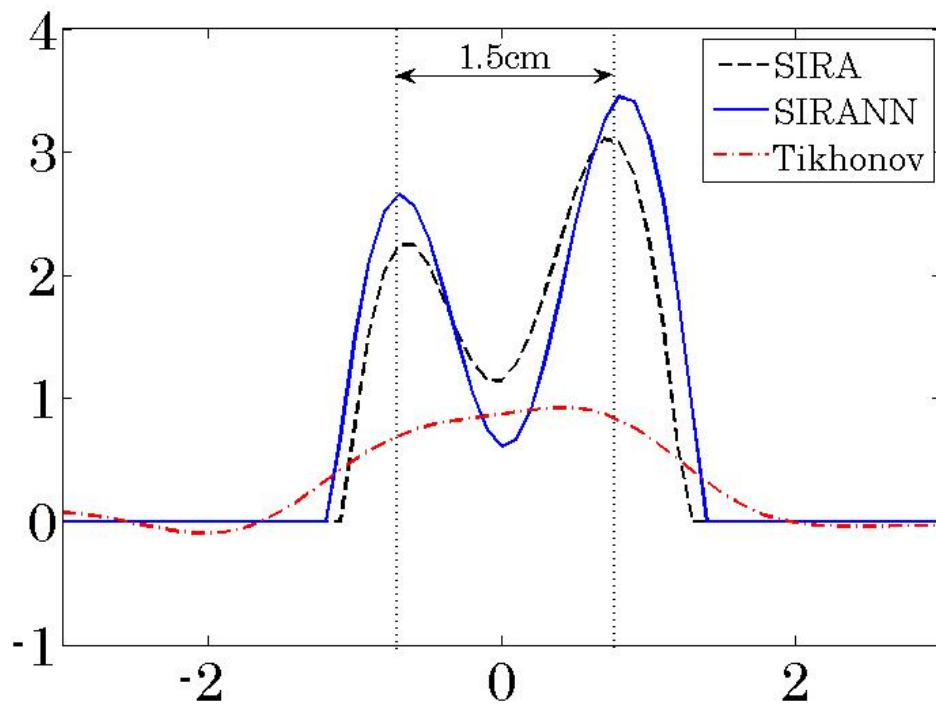


Figure 3.7. Vertical cross sections of reconstructions from SIRA, SIRANN, and Tikhonov method.

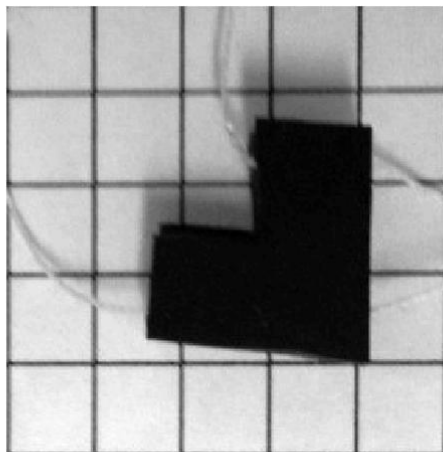


Figure 3.8. Absorber used in the second phantom experiment.

the quality of reconstructed background and object varies among these four cases. Even though S-D pairs with wider separation were removed to minimize strong noise, the reconstructed object in Fig. 3.9(a) by Tikhonov method is surrounded by many background artifacts with a distorted shape of the object. In Fig. 3.9(b), a blur “L” shape object can be roughly identify, but the background is still filled with artifacts. The result in Fig. 3.9(c) reconstructed with SIRA, on the other hand, shows a clearer background and improved object shape. At the end, the reconstruction result from the proposed method, as shown in Fig. 3.9(d), demonstrates that not only the shape of the object is improved to be very similar to the actual one in Fig. 3.8, but also the background noise is further suppressed as compared to the one using SIRA alone.

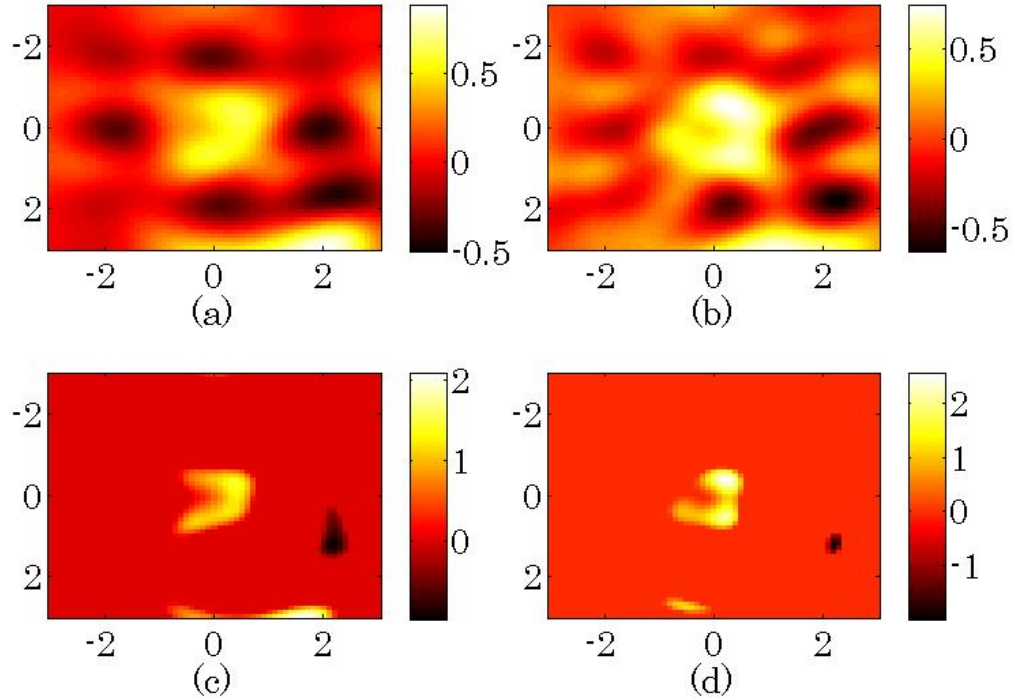


Figure 3.9. The reconstructed image of the phantoms experiment by (a) Tikhonov, (b) GLS, (c)SIRA, and (d) SIRANN method.

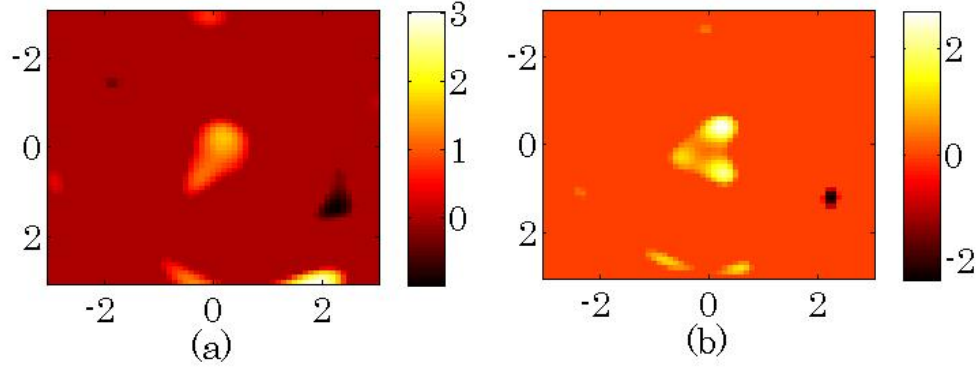


Figure 3.10. The reconstructed image of the phantoms experiment with measurements from the first to seventh nearest S-D pairs by (a) SIRA, and (b) proposed improving method.

In addition, measurements from seventh nearest S-D pairs were included (220 S-D pairs) into the reconstruction process to test the robustness of the proposed method. The results from SIRA and the proposed method with regularization parameter $\lambda = 8 \times 10^{-6}$ and 4×10^{-6} are shown in Fig. 3.10. SSIM and CNR for all the phantom results were calculated and listed in Table 3.2. It is clear that including measurements with lower SNR indeed hurts the reconstruction quality, as the SSIM and CNR values were both decreasing and the reconstructed object deviate further from its original shape. However, with the appropriate weighting coefficients, the object in Fig. 3.10(b), which was reconstructed by the proposed method, still had the similar structure as the original object. On the other hand, the “L”-shape object cannot be identified from the reconstruction of SIRA as in Fig. 3.10(b).

3.2.3 Human Finger Tapping Experiment

Since the results from the simulation and phantom experiments have shown significantly improvements of the reconstruction qualities. It would be interesting to see how our SIRANN method improves the DOT reconstruction with the real

Table 3.2. SSIM and CNR values of phantom reconstructions with Tikhonov, GLS, SIRA, and SIRANN method from 188 measurements as well as with SIRA and SIRANN method from 220 measurements.

Method	SSIM	CNR
Tikhonov	0.32	2.36
GLS	0.34	2.34
SIRA	0.53	4.33
Proposed	0.70	6.61
SIRA (220)	0.41	3.28
Proposed (220)	0.63	5.27

measurements from human brain function studies. A finger tapping experiment is implemented for this purpose.

The experimental protocol was designed as follows: The motor activation epoch consisted of 10 seconds of finger tapping and 20 seconds of rest, which was repeated ten times. The subject was instructed to tap his index and middle fingers against the thumb. The data was acquired using a high-density NIRS system (Cephalogics, LLC.) and the geometry of sources and detectors is illustrated as in Fig. 3.11. The sampling frequency was 10.3 Hz. Hemodynamic changes were averaged over the ten epochs to reduce the noises.

The reconstruction results are shown in Fig. 3.12 with normalized coefficients. Fig. 3.12(a) shows the results with only the sparsity regularization, the objects are moving towards the center and area of objects are too small. On the other hand, Fig.3.12(b) shows the results with both sparsity regularization and the noise normalization with our novel noise quantification method. Even though the corresponding functional MRI image was not available as a reference image, the active regions with proper size can clearly be seen from the image.

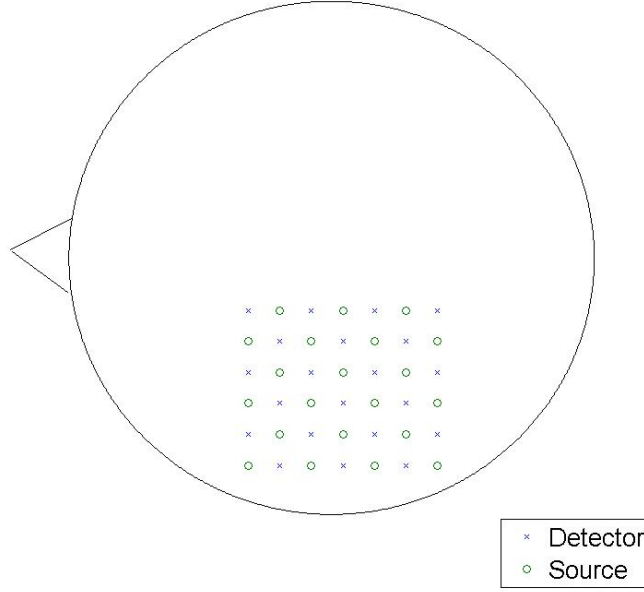


Figure 3.11. Source detector geometry of the finger tapping experiment.

3.3 Conclusion

In this chapter, we developed and demonstrated a practical method to quantify the noise variance for the DOT problem. The noise variance can be estimated from very limited information, which is also easy to obtain. Therefore, this approach is practical for most of the DOT-based brain imaging applications. Moreover, the combination of the proposed noise quantification method and sparsity regularization, i.e. SIRANN, formed an efficient DOT image reconstruction algorithm. Such an algorithm improves the spatial resolution and the shape fidelity considerably, as demonstrated throughout this chapter by the reconstructed images based on computer simulations, laboratory tissue phantom, and real human finger tapping measurements.

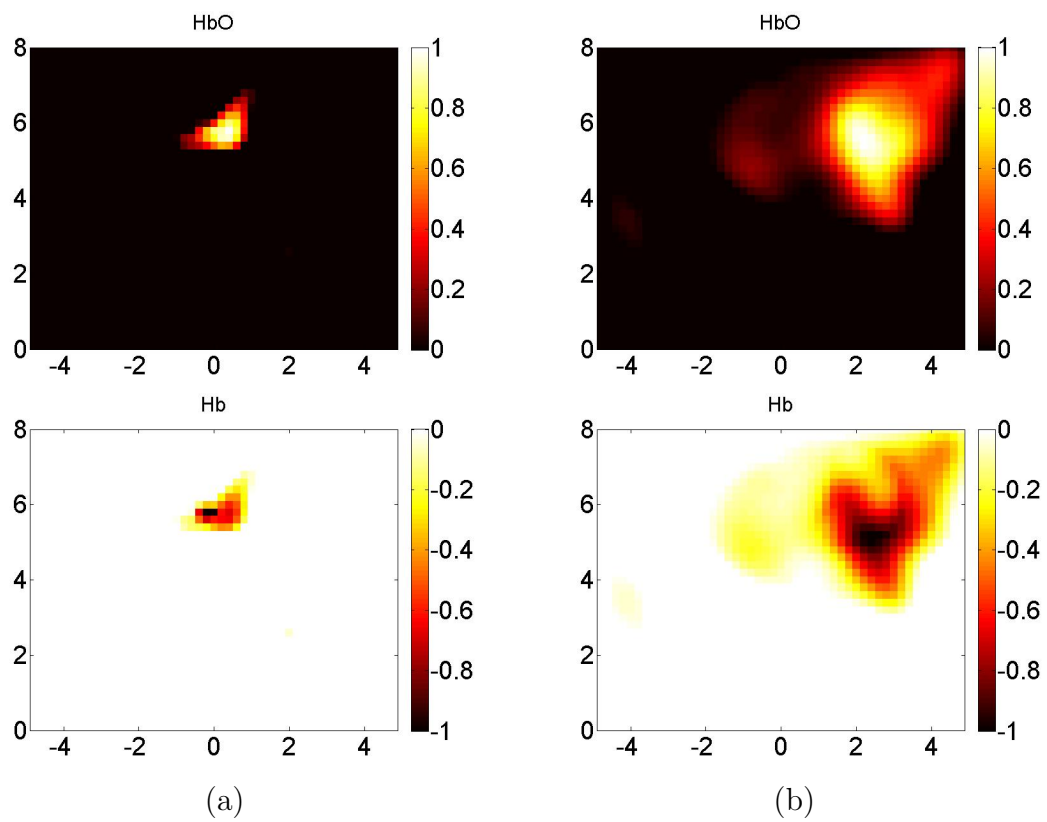


Figure 3.12. Reconstructed images of the finger tapping experiment using (a) Sparsity regularization (b) SIRANN method with the proposed noise model.

CHAPTER 4

DOT RECONSTRUCTION WITH THE RELATIVE NOISE MODEL

Statistical modeling based reconstruction algorithms have also been studied. In the DOT study, two kinds of noise are usually considered in the image reconstruction process: the quantum shot noise and the thermal noise, where the shot noise follows the Poisson distribution and the latter follows Gaussian distribution [8, 64]. Between the two types of noise, the quantum shot noise is usually considered as the dominating [76]. Hence algorithms based on Poisson distribution have been proposed. For example, in [62], an MAP estimator is proposed by modeling the noise-free data as a Markov random process, and the measured time-resolved data as random variables following Poisson distribution.

In this chapter, the pdf of RN is derived and corresponding reconstruction method are discussed.

4.1 The Relative Noise Model

In practice, the raw measurement of reflectance light intensity Φ is always corrupted by noise, i.e. $\tilde{\Phi} = \Phi + w$, where w is the additive noise. Consequently, the measured optical density change in (1.2) becomes:

$$\begin{aligned}
 \widetilde{\Delta OD} &= -\ln \left(\frac{\Phi + w}{\Phi_0} \right) \\
 &= -\ln \left(\frac{\Phi}{\Phi_0} \right) - \ln \left(1 + \frac{w}{\Phi} \right) \\
 &= \Delta OD - \ln \left(1 + \frac{w}{\Phi} \right)
 \end{aligned} \tag{4.1}$$

Hence

$$Y = -\ln(1 + w/\Phi) \quad (4.2)$$

in (4.1) is defined as the relative noise term for the measurement of absorbance change.

Let w be zero mean Gaussian random variable, i.e. $N(0, \sigma_w^2)$. Then w/Φ is also zero mean Gaussian, i.e. $N(0, (\sigma_w/\Phi)^2)$. By assuming the standard deviation of relative noise $\sigma = \sigma_w/\Phi$ is low. In other words, the signal to noise ratio (SNR) of the raw measurement is high. The probability of $(1 + w/\Phi) < 0$ is approximately zero. Therefore, the pdf of Y can be calculated as follows:

$$\begin{aligned} f_Y(y) &= \frac{1}{\sqrt{2\pi}\sigma} \exp\left[-\frac{(e^{-y} - 1)^2}{2\sigma^2}\right] \left|\frac{d(e^{-y} - 1)}{dy}\right| \\ &= \frac{e^{-y}}{\sqrt{2\pi}\sigma} \exp\left[-\frac{(1 - e^{-y})^2}{2\sigma^2}\right]. \end{aligned} \quad (4.3)$$

A computer simulation was performed to validate the derived pdf. In the simulation, 10^6 Gaussian random samples were generated with variance $\sigma^2 = 0.04$. Then all these samples were converted through (4.2). The corresponding normalized histogram was shown in Fig. 4.1. Compared with the derived pdf in (4.3) and the pdf of Gaussian distribution with variance estimated from the samples, it is obvious that the RN pdf fit the histogram better than the Gaussian pdf did.

4.1.1 RN Model Based Reconstruction Formula

Applying the relative noise term to the discretized equation in (1.3) and let $\tilde{\mathbf{b}}$ be the noisy measurement vector, it is straightforward that the RN is given by

$$\mathbf{Y} = \tilde{\mathbf{b}} - \mathbf{b} = \tilde{\mathbf{b}} - \mathbf{A}\mathbf{x}$$

and

$$y_i = \tilde{b}_i - \mathbf{a}_i\mathbf{x}, \quad (4.4)$$

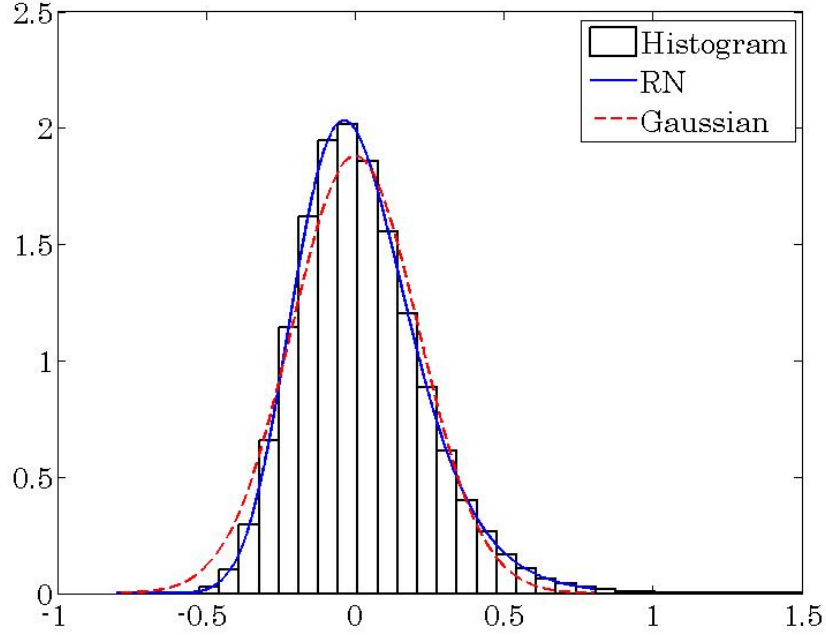


Figure 4.1. Comparison of the derived RN pdf and Gaussian pdf with normalized histogram generated from 10^6 samples.

where y_i and \tilde{b}_i are the i -th element of \mathbf{Y} and of $\tilde{\mathbf{b}}$, respectively, and \mathbf{a}_i is the i -th row of matrix \mathbf{A} .

Before applying the MAP estimation to solve (1.3), with respect to the noise pdf just derived in (4.3). The priori distribution of \mathbf{x} is needed, which consequently will become the regularization terms. As mentioned in Ch2, two types of regularization terms might be used for the DOT reconstruction problem: 1. the group sparsity term; and 2. the combination of ℓ_1 norm and ℓ_2 norm. However, implementing the group sparsity term or the so call ℓ_{21} norm usually leads to a more complicated optimization process, as the regularization term also depends on the design of the size and the structure of the groups. On the other hand, if consider the pdf of \mathbf{x} as a product between the pdf of zero mean Gaussian and zero mean Laplacian with some scaling coefficient (so the total probability remains one), then it leads to a

regularization term consist of both $\|x\|_1$ and $\|x\|_2^2$. The unit circle of ℓ_1 norm, ℓ_2 norm and the combination of the two are illustrated in Fig. 4.2. It shows that the resulting regularization term is a good balance between the ℓ_2 norm, which leads to blurry reconstructions, and the ℓ_1 norm, which might over-sparse the reconstructions.

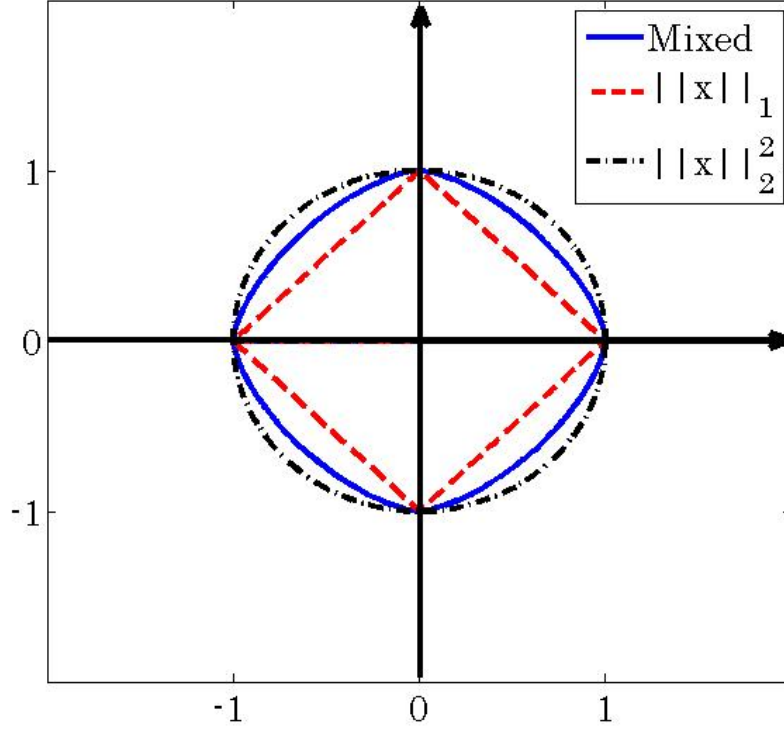


Figure 4.2. The unit circle of ℓ_1 norm (in red dash line), ℓ_2 norm (in black dot-dash line), and the combination of both ℓ_1 norm and ℓ_2 norm (in solid blue line).

Thus, the RN-based reconstruction is formulated as:

$$\hat{\mathbf{x}}_{RN} = \arg \min \left\{ \sum_i \left(y_i + \frac{(e^{-y_i} - 1)^2}{2\sigma_{1_i}^2} \right) + \lambda_1 \|\mathbf{x}\|_1 + \lambda_2 \|\mathbf{x}\|_2^2 \right\}, \quad (4.5)$$

where λ_1 and λ_2 are regularization parameters.

Moreover, in the scenario that the base-line measurement Φ_0 is also affected by the noise, i.e. $\widetilde{\Phi}_0 = \Phi_0 + w_0$, the RN model can also be extended appropriately. In this case the measured optical density change becomes:

$$\begin{aligned}\widetilde{\Delta OD} &= -\ln\left(\frac{\Phi + w}{\Phi_0 + w_0}\right) \\ &= -\ln\left(\frac{\Phi}{\Phi_0}\right) + \ln\left(1 + \frac{w_0}{\Phi_0}\right) - \ln\left(1 + \frac{w}{\Phi}\right) \\ &= \Delta OD + \ln\left(1 + \frac{w_0}{\Phi_0}\right) - \ln\left(1 + \frac{w}{\Phi}\right).\end{aligned}\tag{4.6}$$

Assume both w and w_0 are independent zero-mean Gaussian random variables. It is trivial that both w/Φ and w_0/Φ_0 are also Gaussian. Now define $Y_1 = \ln(1 + w_0/\Phi_0)$, $Y_2 = \ln(1 + w/\Phi)$, and the standard deviation of w_0/Φ_0 and w/Φ as σ_1 and σ_2 , respectively.

The RN in this case is defined as $Z = Y_1 - Y_2$. Therefore, the cdf of Z is given by

$$F_Z(z) = \Pr(\{Y_1 - Y_2 \leq z\}) = \Pr(\{Y_1 - z \leq Y_2\}) = \int_{-\infty}^{\infty} \int_{y_1 - z}^{\infty} f_{Y_1, Y_2}(y_1, y_2) dy_2 dy_1.$$

Therefore,

$$\begin{aligned}f_Z(z) &= \frac{\partial}{\partial z} F_Z(z) \\ &= \int_{-\infty}^{\infty} \frac{e^{y_1}}{\sqrt{2\pi}\sigma_1} \exp\left(-\frac{(1 - e^{y_1})^2}{2\sigma_1^2}\right) \frac{e^{y_1 - z}}{\sqrt{2\pi}\sigma_2} \exp\left(-\frac{(1 - e^{y_1 - z})^2}{2\sigma_2^2}\right) dy_1.\end{aligned}$$

The closed form of $f_Z(z)$ is found as (Refer to Appendix B for the detail of the derivation steps)

$$f_Z(z) = \frac{C}{2\beta} \left(1 - \sqrt{\pi} \exp\left(\frac{\gamma^2}{4\beta}\right) \frac{\gamma}{2\sqrt{\beta}} \operatorname{erfc}\left(\frac{\gamma}{2\sqrt{\beta}}\right)\right),$$

where

$$\begin{aligned} C &= \frac{e^{-z}}{2\pi\sigma_1\sigma_2} \exp\left(-\frac{\sigma_1^2 + \sigma_2^2}{2\sigma_1^2\sigma_2^2}\right) \\ \beta &= \frac{e^{-2z}\sigma_1^2 + \sigma_2^2}{2\sigma_1^2\sigma_2^2} \\ \gamma &= -\frac{e^{-z}\sigma_1^2 + \sigma_2^2}{\sigma_1^2\sigma_2^2}. \end{aligned}$$

Similar to (4.4), the noise of i -th channel in this extended case is defined as $z_i = \tilde{b}_i - \mathbf{a}_i\mathbf{x}$. Then the noise pdf of i -th channel is given by:

$$f_Z(z_i) = \frac{C_i}{2\beta_i} \left(1 - \alpha_i \sqrt{\frac{\pi}{\beta_i}} \exp\left[\frac{\alpha_i^2}{\beta_i}\right] \operatorname{erfc}\left(\frac{\alpha_i}{\sqrt{\beta_i}}\right) \right),$$

where

$$\begin{aligned} C_i &= \frac{e^{-z_i}}{2\pi\sigma_{1_i}\sigma_{2_i}} \exp\left[-\frac{\sigma_{1_i}^2 + \sigma_{2_i}^2}{2\sigma_{1_i}^2\sigma_{2_i}^2}\right] \\ &= \frac{e^{-z_i}}{2\pi\sigma_{1_i}^2 s_i} \exp\left[-\frac{1 + s_i^2}{2s_i^2\sigma_{1_i}^2}\right], \\ \beta_i &= \frac{e^{-2z_i}\sigma_{1_i}^2 + \sigma_{2_i}^2}{2\sigma_{1_i}^2\sigma_{2_i}^2} \\ &= \frac{e^{-2z_i} + s_i^2}{2s_i^2\sigma_{1_i}^2}, \\ \alpha_i &= \frac{\gamma}{2} \\ &= -\frac{e^{-z_i}\sigma_{1_i}^2 + \sigma_{2_i}^2}{2\sigma_{1_i}^2\sigma_{2_i}^2} \\ &= -\frac{e^{-z_i} + s_i^2}{2s_i^2\sigma_{1_i}^2}. \\ s_i &= \sigma_{2_i}/\sigma_{1_i} \end{aligned}$$

Therefore, the corresponding MAP estimator in this case can be found as follows:

$$\begin{aligned} \arg \min \{ & - \sum_i \left(z_i + 1.5 \ln(e^{-2z_i} + s_i^2) - \ln(e^{-z_i} + s_i^2) + \frac{(1 - e^{-z_i})^2}{2\sigma_{1_i}^2 (e^{-2z_i} + s_i^2)} \right) \\ & + \lambda_1 \|\mathbf{x}\|_1 + \lambda_2 \|\mathbf{x}\|_2^2 \} \end{aligned} \quad (4.7)$$

4.2 Optimization Problem

For the RN estimator in (4.5), the sub-gradient of (4.5) can be found as:

$$\nabla f(\mathbf{x}) = - \sum_{i=1}^M (1 - e^{-y_i}(e^{-y_i} - 1)/\sigma_{1_i}^2) \mathbf{a}_i^T + \lambda_1 \frac{\partial \|\mathbf{x}\|_1}{\partial \mathbf{x}} + 2\lambda_2 \mathbf{x}.$$

Similarly, the sub-gradient of RN estimator in (4.7) is:

$$\begin{aligned} \nabla f(\mathbf{x}) = & - \sum_i \left(1 - \frac{3e^{-2z_i}}{(e^{-2z_i} + s_i^2)} + \frac{e^{-z_i}}{(e^{-z_i} + s_i^2)} - \frac{e^{-z_i}(1 - e^{-z_i})(s_i^2 + e^{-z_i})}{\sigma_{1_i}^2 (s_i^2 + e^{-2z_i})^2} \right) \mathbf{a}_i^T \\ & + \lambda_1 \frac{\partial \|\mathbf{x}\|_1}{\partial \mathbf{x}} + 2\lambda_2 \mathbf{x}. \end{aligned}$$

Note that, the ℓ_1 norm term is defined as $\|\mathbf{x}\|_1 = \sum_n |x_n|$, which is the sum of the absolute values. It is straightforward that the absolute value function is a non-smooth function, therefore it is not differentiable. To make the cost function differentiable, the absolute value is approximated by a smooth function: $|x| \approx \sqrt{x \times x + \xi}$, where ξ is a positive smoothing parameter[53]. Then the sub-gradient of the absolute value function can be calculated as $d|x|/dx \approx x/\sqrt{x \times x + \xi}$ and the sub-gradient of the ℓ_1 norm can therefore be easily derived.

However, due to the $(e^{-y_i} - 1)^2$ term in (4.5) and the $(1 - e^{-z_i})^2$ term in (4.7), cost functions of RN estimator in both cases are not convex, but quasiconvex [11] as illustrated by an example in Fig.4.3 for $\mathbf{x} \in \mathbb{R}^2$.

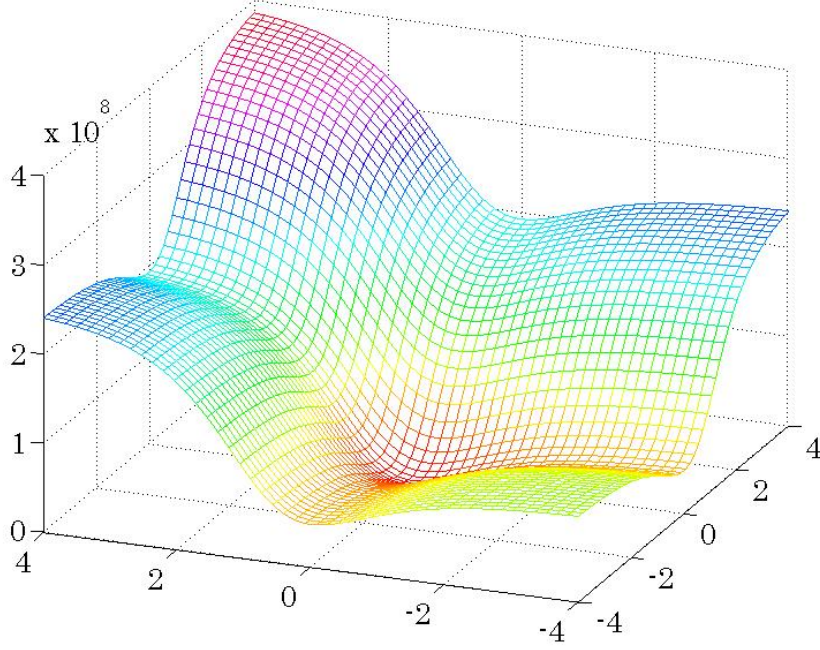


Figure 4.3. An example of the RN cost function with $x \in \mathbb{R}^2$.

Hence it cannot be solved by conventional convex optimization algorithms such as steepest descent or gradient descent methods, as these kind of methods can only yield local optimal solutions or stuck in the valley. Moreover, obtaining the inverse Hessian matrices of (4.5) and (4.7) are not feasible. For example the Hessian of the fidelity term of (4.5) is

$$\mathbf{A}^T \begin{pmatrix} \frac{2e^{-2y_1} - e^{-y}}{\sigma_{1_1}^2} & & & \\ & \frac{2e^{-2y_2} - e^{-y}}{\sigma_{1_2}^2} & & \\ & & \ddots & \\ & & & \frac{2e^{-2y_N} - e^{-y}}{\sigma_{1_N}^2} \end{pmatrix} \mathbf{A}.$$

Since the sensing matrix \mathbf{A} has less number of rows than it of columns as well as the non-differentiability of ℓ_1 norm, the Hessian of the cost function is not invertible. As a result, Newton's method cannot be applied neither.

As an alternative, the ellipsoid algorithm is one of the cutting plane methods that can be used to find a steady solution for this kind of optimization problems[29, 17]. The algorithm starts from an initial ellipsoid $\mathbf{P} \in \mathbb{R}^N$, which contains the solution. In each iteration, the gradient at the center of current ellipsoid is calculated, then the half ellipsoid along the gradient direction is cut and removed. Thereafter, a new ellipsoid is updated, which is the smallest ellipsoid that includes the remaining half ellipsoid from the previous step. The pseudo-code is given as follows [7]:

Define the ellipsoid as $E(\mathbf{x}, \mathbf{P}) = \{\mathbf{z} | (\mathbf{z} - \mathbf{x})^T \mathbf{P}^{-1} (\mathbf{z} - \mathbf{x}) \leq 1\}$

Initial an ellipsoid $E(\mathbf{x}, \mathbf{P})$ containing the optimal solution \mathbf{x}^*

repeat

1. $\mathbf{g}^{(k)} \leftarrow \nabla f(\mathbf{x}^{(k)})$
2. if $\sqrt{\mathbf{g}^{(k)T} \mathbf{P}^{(k)} \mathbf{g}^{(k)}} \leq \epsilon$, return $\mathbf{x}^{(k)}$
3. update ellipsoid

$$(a) \quad \mathbf{g}^{(k+1)} \leftarrow \frac{1}{\sqrt{\mathbf{g}^{(k)T} \mathbf{P}^{(k)} \mathbf{g}^{(k)}}} \mathbf{g}^{(k)}$$

$$(b) \quad \mathbf{x}^{(k+1)} \leftarrow \mathbf{x}^{(k)} - \frac{1}{N+1} \mathbf{P}^{(k)} \mathbf{g}^{(k+1)}$$

$$(c) \quad \mathbf{P}^{(k+1)} \leftarrow \frac{N^2}{N^2-1} \left(\mathbf{P}^{(k)} - \frac{2}{N+1} \mathbf{P}^{(k)} \mathbf{g}^{(k+1)} \mathbf{g}^{(k+1)T} \mathbf{P}^{(k)} \right)$$

Therefore, the optimal solution of (4.5) and (4.7) can be obtained with only the first order sub-gradient of the cost functions.

4.3 Experimental Results

To demonstrate the improvement in reconstructed images by using RN estimator as compared to other Gaussian model based least square methods, both simulation experiment and phantom experiments were performed and illustrated in this section.

4.3.1 Simulated Data

First, a computer simulation experiment was designed to show the improvement of RN estimator compared to conventional least square methods. Similar to previous simulation experiments, in this experiment, twenty five bifurcated optodes were placed as a 5×5 square grid over the top surface of a semi-infinite medium and centered at the origin as illustrated in Fig.2.2. The separation between every two nearest optodes was 1.4 cm. To avoid low SNR channels, only the first to sixth nearest S-D pairs were used. Consequently, 188 channels can be obtained.

The absorption and reduced scattering coefficients of the homogeneous background medium were chosen to be $\mu_{a_0} = 0.06 \text{ cm}^{-1}$ and $\mu_{s_0} = 8.2 \text{ cm}^{-1}$, respectively [16]. Since only the relative absorption changes from the background are considered, a “U” shape absorber with $\Delta\mu_a = 0.6 \text{ cm}^{-1}$ was placed at the center of a relative zero background as shown in Fig.4.4(a), 1.5 cm below the measuring plane. White Gaussian noise was added the inhomogeneous measurements Φ .

In this example, since the number of non-zero pixels in the original image was greater than twenty five, which was the number of optodes, both ℓ_1 norm and ℓ_2 norm terms were used to regularize the solution. The stopping criterion for the corresponding ellipsoid algorithm was set as $\epsilon < 10^{-10}$ with the initial ellipsoid $\mathbf{P} = 10\mathbf{I}$, where \mathbf{I} is the identity matrix.

To demonstrate the improvement of the RN estimator, the reconstruction was also compared with Tikhonov method as in (1.4) and least square with both ℓ_1 norm and ℓ_2 norm regularization (LSL12) as in the following equation:

$$\hat{\mathbf{x}} = \arg \min_{\mathbf{x}} \{ \|\mathbf{Ax} - \mathbf{b}\|_2^2 + \lambda_1 \|\mathbf{x}\|_1 + \lambda_2 \|\mathbf{x}\|_2^2 \}.$$

In addition, even though the noise added to the inhomogeneous measurements was WGN, the variance of the RN term are different among different channels as discussed

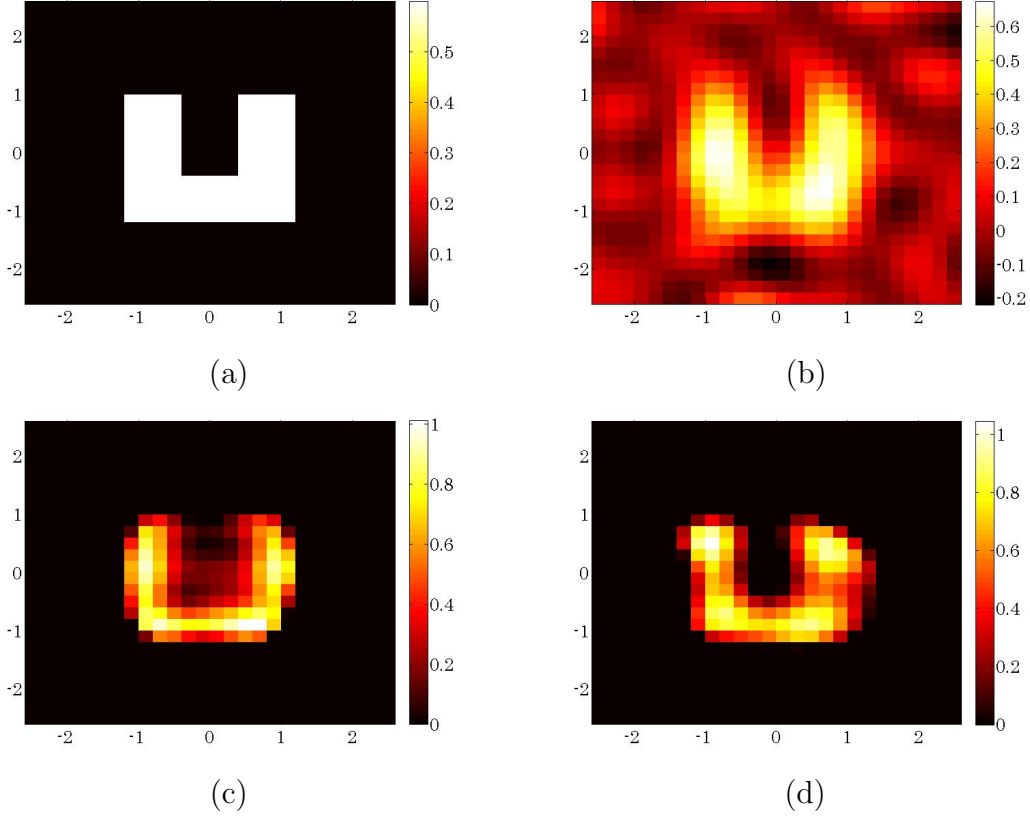


Figure 4.4. (a) The original image used for the simulation, and comparison of the reconstructions with: (b) Tikhonov; (c) LSL12; (d) RN estimator..

in Ch.3 Hence the fidelity term of both Tikhonov method and LSL12 method should be re-weighted before the reconstruction step as [80]

$$\|\mathbf{D}(\mathbf{Ax} - \mathbf{b})\|_2^2,$$

where \mathbf{D} is a diagonal matrix with the entries equal to the reciprocal of noise standard deviation of each corresponding channel. Followed by (3.11), the noise variance of the i -th channel can be calculated as

$$\sigma_{w(i)}^2 \approx \frac{\sigma^2}{\phi^2(i)} + \frac{5}{2} \frac{\sigma^4}{\phi^4(i)} + \frac{32}{3} \frac{\sigma^6}{\phi^6(i)} + O(\sigma_w^8),$$

where σ^2 is the variance of noise added to $\phi(i)$

As we expected, the reconstructed image by Tikhonov, as shown in Fig.4.4(b), was still blurry and horizontal bar was barely recovered. Improvement of spatial resolution can be observed from the result of LSL12 method as shown in Fig.4.4(c), but the area inside the object is still noisy or two vertical bars of the object was not fully separated. The reconstructed image shown in Fig.4.4(d) was obtained from the proposed RN estimator, where not only was the spatial resolution promoted, but also the shape of reconstructed object was almost the same as the original one. The cross section profiles at $y=0$ are shown in Fig.4.5 to further illustrate the improvement of RN estimator.

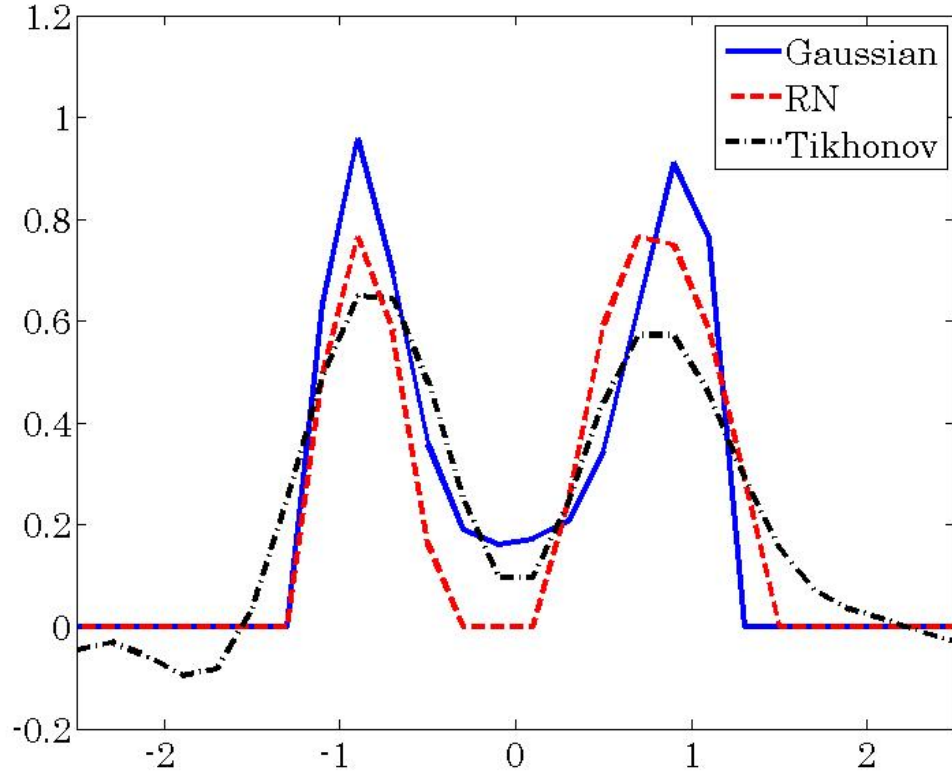


Figure 4.5. Cross section profile of reconstructions from LSL12, RN, and Tikhonov method.

Similar to the previous chapter, two quantitative metrics, SSIM and CNR, were computed to show the improvement of RN estimator over other reconstruction methods. The SSIM and the CNR of all the three reconstruction methods were computed and listed in Table 4.1. Notice that the SSIM from the RN estimator was the highest among all the methods that have been tested, which means due to the more accurate noise model, the structural of the object in the reconstructed image was the most accurate one among all the methods tested.

Table 4.1. SSIM and CNR values of simulation reconstructions with Tikhonov, LSL12, and proposed RN estimator.

Method	SSIM	CNR
Tikhonov	0.8449	4.5242
LSL12	0.8576	4.7156
RN	0.8709	4.9380

The high CNR indicates that most of the non-zero pixels are located in the ROI. The proposed RN estimator recovered the object almost completely with a clean background both inside and outside the U shape object, therefore the CNR was the highest among all the methods.

4.3.2 Phantom Data

Next, the phantom experiment in the previous chapter was used to evaluate RN estimator with real measurements. In this phantom experiment, the experimental setup and procedures were similar to those used in [59], where a CW-based DOT imaging system (DYNOT, NIRx, New York) was used to obtain the measurements from a container of $15 \times 10 \times 10$ cm³ filled with 1% Intralipid solution. The optodes

were placed on the very top surface of the intralipid solution such that the tips of optodes were just touching the liquid phantom surface. In this way, no air gap existed between the tips and liquid to minimize the refractive index (RI) mismatch. This setup provided us with a very similar boundary condition to that in light-tissue interaction situation. Thus, our experimental setup did not deviate too much from the traditional light-tissue interaction setup. The absorption and reduced scattering coefficients of the homogeneous background medium were $\mu_{a0} = 0.08 \text{ cm}^{-1}$ and $\mu_{s0} = 8.8 \text{ cm}^{-1}$, respectively. An “L” shape absorber as shown in Fig.3.8 was placed 1.5cm under the surface with the grid size on the background was $5\text{mm} \times 5\text{mm}$.

Since the absorber was thin along the depth direction, 2D reconstruction at the depth of 1.5cm was considered. The pixel size was set as $2\text{mm} \times 2\text{mm}$. In this experiment, the number of non-zero pixels in the reconstruction was not as small as the number of optodes used, hence both ℓ_1 norm and ℓ_2 norm regularization terms should be applied.

The measured data was first reconstructed by Tikhonov method with regularization parameter $\lambda = 10^{-5.2}$ as shown in Fig??(a). Similar to the simulation, the reconstructed object has larger size than the actual one with unclear boundary. By selecting $\lambda_1 = 10^{-4.6}$ and $\lambda_2 = 10^{-6}$, the reconstruction result of the LSL1 is shown in Fig??(b). In the reconstructed image, despite the background noise shown in the bottom and the lower right corner of the image, the horizontal bar of the object was successfully recovered. However, the top of the vertical bar was bent toward left and tended to merge into the left end of the object.

In comparison, the reconstruction of proposed RN estimator in (4.5) with $\lambda_1 = 10^{-5}$ and $\lambda_2 = 10^{-6}$ is shown in Fig.4.6(b). Even though the background noise in the lower right corner was not completely suppressed, background noise in the bottom of the image was successfully removed and the shape of the reconstructed object is

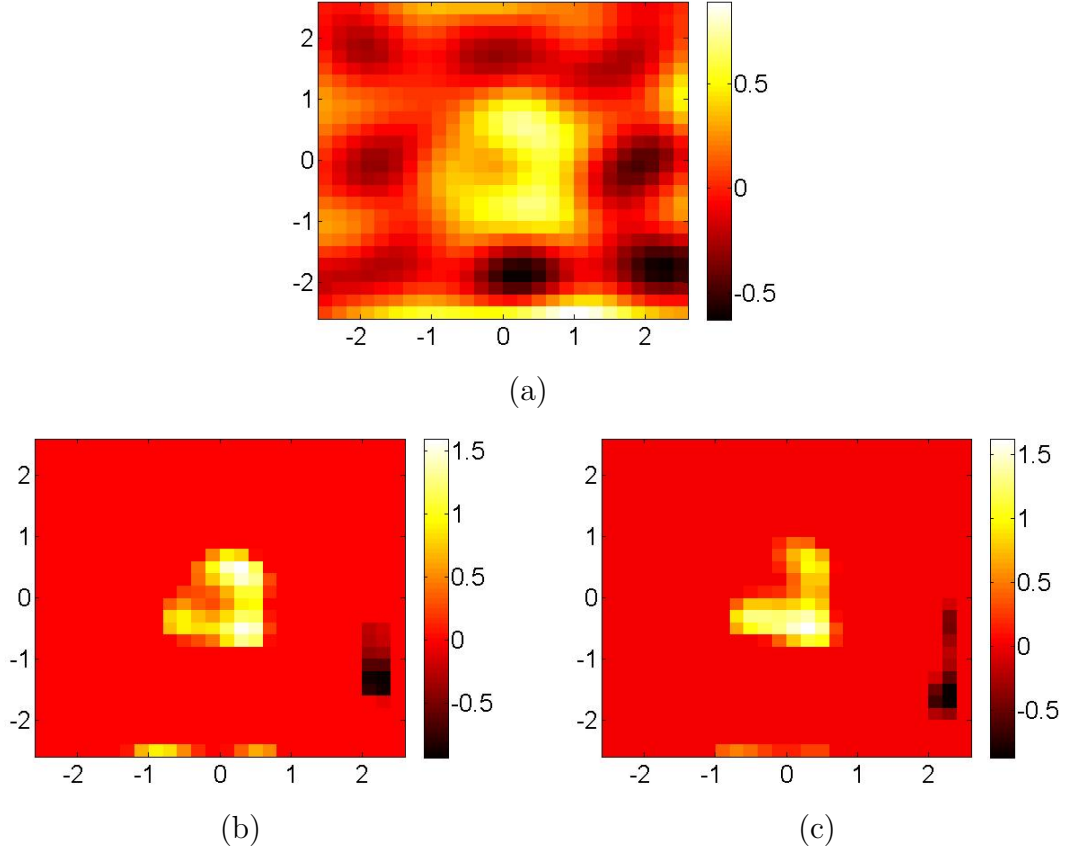


Figure 4.6. Reconstructions of phantom experimental data by:(a)Tikhonov (b)LSL12; (b)RN estimator..

almost identical as the absorber used. In other words, the proposed RN estimator did improve the fidelity of reconstructed images. The SSIM and CNR values were also computed and listed in Table.4.2

4.3.3 Parameter Selection

The regularization parameter for Tikhonov method can be found by the L-curve method [77]. For the RN estimator and LSL12, the optimal values of two regularization parameters are vary among different experiments and different fidelity terms. However our experience showed that a good rule of thumb to deal with them

Table 4.2. SSIM and CNR values of phantom reconstructions with LSL12, and proposed RN estimator.

Method	SSIM	CNR
LSL12	0.8042	6.1709
RN	0.8809	8.4553

is to fix the ratio between the two as a constant first, e.g. $\lambda_2 = c \times \lambda_1$, then adjusting only one regularization parameter is needed in order to found the best reconstruction results. In practice, the constant ratio $c < 1$ can first be tuned through few number of trails to find a good balance between reconstructed objects being too sparse (c is too small) and too blurry (c is too large). Then with the constant ratio c fixed, the optimal value of λ_1 can be found through strategies like the L-curve method. For instances, in the result shown in Fig4.6(b), the constant $c = 0.1$ was found.

4.4 Conclusion

In this chapter, an RN noise model was derived by considering the modified Beer-Lambert law and Rytov linear approximation. Thereafter, an effective MAP estimator was developed based on the derived RN noise model. Together with both ℓ_1 norm and ℓ_2 norm regularization terms, an effective reconstruction formula for CW DOT was obtained. Although the corresponding optimization problem is quasi-convex, it can be solved by ellipsoid algorithm. With the proposed reconstruction formula, the shape of the reconstructed object is more accurate as compared to the conventional least square scheme with the same regularizer as demonstrated with both computer simulation and the real laboratory measurements.

CHAPTER 5

SUMMARY AND FUTURE DIRECTIONS

5.1 Summary

In this work, sparsity enhanced reconstructing algorithms have been developed to improve the reconstruction quality for DOT.

The sparsity regularized 3D reconstruction algorithm corrects the sensitivity attenuation of the forward matrix by using the maximum singular values of submatrices relate to different depths. Such algorithm presented great reconstruction results under the WGN condition.

By considering the measurement acquisition process of DOT, the relative noise was discovered. Two reconstruction algorithms have developed accordingly.

The first method approximated the RN as Gaussian noise with different variances among the measuring channels. The corresponding variance quantification formula was derived. The combination of sparsity constraint and the noise whitening with the developed noise quantification method improve the shape fidelity of a reconstructed object, as it can be identified almost correctly even with noisy measurements. Utilizing this novel noise quantification method in the noise whitening process along with the sparsity constraint brought the sparsity regularized DOT reconstruction into an even more practical level.

The statistical distribution of RN has also been derived. The second reconstruction formula was obtained by applying the MAP framework to the derived RN pdf and combined with the sparsity constraint. Even though the resulting cost function is not convex, it has been solved by ellipsoid algorithm. Due to the more precise

statistical information, objects recovered by this formula have shown almost identical shapes as the original ones.

The advantage of noise quantification based reconstruction method is that the least square related cost functions have been studied extensively and therefore can be solved by a number of advanced optimization algorithms in an effective way. Consequently, reconstruction images can be obtain in a short amount of time with almost correct shape of objects. Hence it can be used for fast reconstruction with slightly lower quality than the RN estimator or when the variance of the raw noise is not available. On the other hand, the RN pdf based method indeed recovered the shape of targeting objects correctly, the convergence speed of ellipsoid algorithm is extremely slow. Hence it is not feasible to deal with image with a large amount of pixels. Therefore, it can be used to reconstruct small images with relatively higher quality.

5.2 Future Directions

5.2.1 Improve the Reconstruction Speed of RN Model Formula

Implementation of the ellipsoid algorithm is discussed in Appendix C. Even though implementing the algorithm in C with the general BLAS library can boost the speed approximately 5 times faster (could be even faster with the ATLAS) than the MATLAB version, the convergence rate of the ellipsoid algorithm is still extremely slow. A further acceleration might be achieved by solving the matrix operations parallelly on GPU, but the gain in speed is still limited due to the nature of ellipsoid algorithm that the volume reduction factor degrades significantly as the number of pixels become large. For this reason, a more efficient algorithm to solve (4.5) is needed to reconstruct larger images in a timely manner. The conventional way to speed up a gradient based algorithm, e.g. steepest descent, is to change the coordinate by

the inverse of Hessian, i.e. Newton's method. However, the Hessian of the fidelity term is singular as the sensing matrix is under-determined hence it is not invertible. Moreover, the ℓ_1 norm term is not differentiable, therefore its Hessian cannot be found. Methods to approximate the Newton's step for convex optimization problems has been studied and many newly developed algorithms have been proposed. It is possible that some of these developed algorithm can be used to solve the quasi-convex problem (4.5) effectively. One other possible way to approximate the Hessian is to replace it by the ellipsoid matrix found after a number of initial iterations of ellipsoid algorithm.

5.2.2 Combine the Physiological Noise Into the RN Model

As discussed earlier, two types of noise can shield the true response signals and mislead to wrong conclusions when DOT is utilized to study in vivo brain activities stimulated under given tasks. The first type of noise is the instrument noise, which is the type of noise considered in this thesis. The second type of the noise is physiological variations. For example heartbeat, respiration, and even motion of the patient. These types of noise are usually considered as band-limited Gaussian noise. It is possible to extend the RN model to further reduce the physiological noise by looking into the properties of it, e.g. frequency range of different types of physiological signals.

5.2.3 Develop a More Effective Method to Find the Optimal Regularization Parameters When Both ℓ_1 Norm and ℓ_2 Norm are Used

Generally speaking, the regularization parameter is selected empirically. For selecting only one parameter, there are many methods that is already available and are relatively easy to find. In the RN model formula, even though we can fixed the ratio between the two regularization parameters to reduce the number of tuning

parameters, finding the appropriate ratio is still empirical. It is desire to develop a more effective way or automatic way to approximate the optimal regularization parameters.

APPENDIX A

Acronyms

2-D	Two-Dimensional
3-D	Three-Dimensional
ALM	augmented Lagrangian method
AM	Amplitude Modulated
ATLAS	Automatically Tuned Linear Algebra Software
BLAS	Basic Linear Algebra Subprograms
BKG	Background
CDF	Cumulative Distribution Function
CNR	Contrast to Noise Ratio
CS	Compressive Sensing
CT	Computed Tomography
CW	Continuous-Wave
DA	Diffusion Approximation
DCA	Depth Compensation Algorithm
DOT	Diffuse Optical Tomography
EM	Expectation Maximization
FOV	Field Of View
GCV	Generalized Cross Validation
GLS	Generalized Least Square
GPU	Graphics Processing Unit
Hb	Deoxygenated Hemoglobin
HbO	Oxygenated Hemoglobin
LAPACK	Linear Algebra PACKage
LSL12	least square with both ℓ_1 norm and ℓ_2 norm regularization
MAP	Maximum A Posteriori
MRI	Magnetic resonance imaging
NIR	Near InfraRed

PDF	Probability Distribution Function
RI	Refractive Index
RN	Relative Noise
ROI	Region Of Interest
SALSA	Split Augmented Lagrangian Shrinkage Algorithm
S-D	Source-Detector
SIRA	Sparse Image Reconstruction Algorithm
SIRANN	Sparse Image Reconstruction Algorithm with Noise Normalization
SNR	Signal-to-Noise Ratio
SPD	Symmetric Positive Definite
SSIM	Structural Similarity Index Metric
TV	Total Variation
WGN	White Gaussian Noise

APPENDIX B

Derivation of RN pdf When Both Inhomogeneous and Background Measurements
Are Corrupted by Noise

Derivation of the RN pdf in the scenario that the both base-line measurement Φ_0 and inhomogeneous measurement Φ are affected by the Gaussian noise is shown in this Appendix. The corresponding cost function and its first order derivative are also discussed.

In this case the measured optical density change becomes:

$$\begin{aligned}\widetilde{\Delta OD} &= -\ln\left(\frac{\Phi + w}{\Phi_0 + w_0}\right) \\ &= -\ln\left(\frac{\Phi}{\Phi_0}\right) + \ln\left(1 + \frac{w_0}{\Phi_0}\right) - \ln\left(1 + \frac{w}{\Phi}\right) \\ &= \Delta OD + \ln\left(1 + \frac{w_0}{\Phi_0}\right) - \ln\left(1 + \frac{w}{\Phi}\right).\end{aligned}\tag{B.1}$$

Assume both w and w_0 are independent zero-mean Gaussian random variables. It is trivial that both w/Φ and w_0/Φ_0 are also Gaussian. Now define $Y_1 = \ln(1 + w_0/\Phi_0)$, $Y_2 = \ln(1 + w/\Phi)$, and the standard deviation of w_0/Φ_0 and w/Φ as σ_1 and σ_2 , respectively.

The relative noise in this case is defined as $Z = Y_1 - Y_2$. Therefore, the cdf of Z is given by

$$F_Z(z) = \Pr(\{Y_1 - Y_2 \leq z\}) = \Pr(\{Y_1 - z \leq Y_2\}) = \int_{-\infty}^{\infty} \int_{y_1 - z}^{\infty} f_{Y_1, Y_2}(y_1, y_2) dy_2 dy_1.$$

Therefore,

$$\begin{aligned}f_Z(z) &= \frac{\partial}{\partial z} F_Z(z) \\ &= \int_{-\infty}^{\infty} \frac{\partial}{\partial z} \left[\int_{y_1 - z}^{\infty} f_{Y_1, Y_2}(y_1, y_2) dy_2 \right] dy_1 \\ &= \int_{-\infty}^{\infty} [0 + 0 - f_{Y_1, Y_2}(y_1, y_1 - z)(-1)] dy_1 \\ &= \int_{-\infty}^{\infty} \frac{e^{y_1}}{\sqrt{2\pi}\sigma_1} \exp\left(-\frac{(1 - e^{y_1})^2}{2\sigma_1^2}\right) \frac{e^{y_1 - z}}{\sqrt{2\pi}\sigma_2} \exp\left(-\frac{(1 - e^{y_1 - z})^2}{2\sigma_2^2}\right) dy_1.\end{aligned}$$

Hence, the pdf of the relative noise Z is given by

$$\begin{aligned} f_Z(z) &= \int_{-\infty}^{\infty} \frac{e^{2y_1-z}}{2\pi\sigma_1\sigma_2} \exp\left(-\frac{\sigma_2^2(1-e^{y_1})^2 + \sigma_1^2(1-e^{y_1-z})^2}{2\sigma_1^2\sigma_2^2}\right) dy_1. \\ &= C \int_{-\infty}^{\infty} e^{2y_1} e^{-\beta e^{2y_1} - \gamma e^{y_1}} dy_1, \end{aligned}$$

where

$$\begin{aligned} C &= \frac{e^{-z}}{2\pi\sigma_1\sigma_2} \exp\left(-\frac{\sigma_1^2 + \sigma_2^2}{2\sigma_1^2\sigma_2^2}\right) \\ \beta &= \frac{e^{-2z}\sigma_1^2 + \sigma_2^2}{2\sigma_1^2\sigma_2^2} \\ \gamma &= -\frac{e^{-z}\sigma_1^2 + \sigma_2^2}{\sigma_1^2\sigma_2^2}. \end{aligned}$$

Let $x = e^{y_1}$. The integral therefore becomes

$$f_Z(z) = C \int_0^{\infty} x^2 e^{-\beta x^2 - \gamma x} x^{-1} dx = C \int_0^{\infty} x e^{-\beta x^2 - \gamma x} dx. \quad (\text{B.2})$$

Checking the tables from [39], we find that

$$\int_0^{\infty} x^{\nu-1} e^{-\beta x^2 - \gamma x} dx = (2\beta)^{-\nu/2} \Gamma(\nu) \exp\left(\frac{\gamma^2}{8\beta}\right) D_{-\nu}\left(\frac{\gamma}{\sqrt{2\beta}}\right), \quad \beta > 0, \nu > 0, \quad (\text{B.3})$$

where $D_{-\nu}(x)$ is the parabolic cylinder function.

Note that $f_Z(z)$ in (B.2) is a special case of (B.3) when $\nu = 2$. Hence, $f_Z(z)$ in (B.2) is simplified as

$$\begin{aligned} f_Z(z) = C \int_0^{\infty} x e^{-\beta x^2 - \gamma x} dx &= C(2\beta)^{-1} \Gamma(2) \exp\left(\frac{\gamma^2}{8\beta}\right) D_{-2}\left(\frac{\gamma}{\sqrt{2\beta}}\right) \\ &= \frac{C}{2\beta} \exp\left(\frac{\gamma^2}{8\beta}\right) D_{-2}\left(\frac{\gamma}{\sqrt{2\beta}}\right), \end{aligned}$$

where C, β, γ are defined as above.

Applying Eq 9.254-2 in [39]:

$$\begin{aligned}
D_{-2}(z) &= e^{\frac{z^2}{4}} \sqrt{\frac{\pi}{2}} \left\{ \sqrt{\frac{2}{\pi}} e^{-\frac{z^2}{2}} - z \left[1 - \Phi \left(\frac{z}{\sqrt{2}} \right) \right] \right\} \\
&= e^{-\frac{z^2}{4}} - e^{\frac{z^2}{4}} \sqrt{\frac{\pi}{2}} z \operatorname{erfc} \left(\frac{z}{\sqrt{2}} \right) \\
D_{-2} \left(\frac{\gamma}{\sqrt{2\beta}} \right) &= \exp \left(-\frac{\gamma^2}{8\beta} \right) - \exp \left(\frac{\gamma^2}{8\beta} \right) \sqrt{\pi} \frac{\gamma}{2\sqrt{\beta}} \operatorname{erfc} \left(\frac{\gamma}{2\sqrt{\beta}} \right)
\end{aligned}$$

Hence the closed form of $f_Z(z)$ is given by

$$\begin{aligned}
f_Z(z) &= \frac{C}{2\beta} \exp \left(\frac{\gamma^2}{8\beta} \right) D_{-2} \left(\frac{\gamma}{\sqrt{2\beta}} \right) \\
&= \frac{C}{2\beta} \exp \left(\frac{\gamma^2}{8\beta} \right) \left(\exp \left(-\frac{\gamma^2}{8\beta} \right) - \exp \left(\frac{\gamma^2}{8\beta} \right) \sqrt{\pi} \frac{\gamma}{2\sqrt{\beta}} \operatorname{erfc} \left(\frac{\gamma}{2\sqrt{\beta}} \right) \right) \\
&= \frac{C}{2\beta} \left(1 - \sqrt{\pi} \exp \left(\frac{\gamma^2}{4\beta} \right) \frac{\gamma}{2\sqrt{\beta}} \operatorname{erfc} \left(\frac{\gamma}{2\sqrt{\beta}} \right) \right)
\end{aligned}$$

Similar to (4.4), the noise of i -th channel in this extended case is defined as $z_i = \tilde{b}_i - \mathbf{a}_i \mathbf{x}$. Then the noise pdf of i -th channel is given by:

$$f_Z(z_i) = \frac{C_i}{2\beta_i} \left(1 - \alpha_i \sqrt{\frac{\pi}{\beta_i}} \exp \left[\frac{\alpha_i^2}{\beta_i} \right] \operatorname{erfc} \left(\frac{\alpha_i}{\sqrt{\beta_i}} \right) \right),$$

where

$$\begin{aligned}
C_i &= \frac{e^{-z_i}}{2\pi\sigma_{1_i}\sigma_{2_i}} \exp \left[-\frac{\sigma_{1_i}^2 + \sigma_{2_i}^2}{2\sigma_{1_i}^2\sigma_{2_i}^2} \right] \\
&= \frac{e^{-z_i}}{2\pi\sigma_{1_i}^2 s_i} \exp \left[-\frac{1 + s_i^2}{2s_i^2\sigma_{1_i}^2} \right], \\
\beta_i &= \frac{e^{-2z_i}\sigma_{1_i}^2 + \sigma_{2_i}^2}{2\sigma_{1_i}^2\sigma_{2_i}^2} \\
&= \frac{e^{-2z_i} + s_i^2}{2s_i^2\sigma_{1_i}^2}, \\
\alpha_i &= \frac{\gamma}{2} \\
&= -\frac{e^{-z_i}\sigma_{1_i}^2 + \sigma_{2_i}^2}{2\sigma_{1_i}^2\sigma_{2_i}^2} \\
&= -\frac{e^{-z_i} + s_i^2}{2s_i^2\sigma_{1_i}^2}. \\
s_i &= \sigma_{2_i}/\sigma_{1_i}
\end{aligned}$$

Therefore, the MAP estimator in this case can be found as follows:

$$\begin{aligned}
&\arg \max \{ \ln f_W(\tilde{\mathbf{b}} - \mathbf{A}\mathbf{x}) - \lambda_1 \|\mathbf{x}\|_1 - \lambda_2 \|\mathbf{x}\|_2^2 \} \\
&= \arg \min \{ -\sum \ln \frac{C_i}{2\beta_i} - \sum \ln \left(1 - \alpha_i \sqrt{\frac{\pi}{\beta_i}} \exp \left[\frac{\alpha_i^2}{\beta_i} \right] \operatorname{erfc} \left(\frac{\alpha_i}{\sqrt{\beta_i}} \right) \right) + \lambda_1 \|\mathbf{x}\|_1 + \lambda_2 \|\mathbf{x}\|_2^2 \} \\
&\approx \arg \min \{ -\sum \ln \frac{C_i}{2\beta_i} - \sum \ln \left(-\alpha_i \sqrt{\frac{\pi}{\beta_i}} \exp \left[\frac{\alpha_i^2}{\beta_i} \right] \operatorname{erfc} \left(\frac{\alpha_i}{\sqrt{\beta_i}} \right) \right) + \lambda_1 \|\mathbf{x}\|_1 + \lambda_2 \|\mathbf{x}\|_2^2 \} \\
&\text{(Since } \left(-\alpha_i \sqrt{\frac{\pi}{\beta_i}} \exp \left[\frac{\alpha_i^2}{\beta_i} \right] \operatorname{erfc} \left(\frac{\alpha_i}{\sqrt{\beta_i}} \right) \right) \gg 1) \\
&= \arg \min \{ \sum_i \left(z_i + 1.5 \ln(e^{-2z_i} + s_i^2) - \ln(e^{-z_i} + s_i^2) - \frac{\alpha_i^2}{\beta_i} - \ln \left(\operatorname{erfc} \left(\frac{\alpha_i}{\sqrt{\beta_i}} \right) \right) + \frac{1 + s_i^2}{2s_i^2\sigma_{1_i}^2} \right) + \right. \\
&\quad \left. \lambda_1 \|\mathbf{x}\|_1 + \lambda_2 \|\mathbf{x}\|_2^2 \right\} \\
&\approx \arg \min \{ \sum_i \left(z_i + 1.5 \ln(e^{-2z_i} + s_i^2) - \ln(e^{-z_i} + s_i^2) - \frac{(e^{-z_i} + s_i^2)^2}{2s_i^2\sigma_{1_i}^2(e^{-2z_i} + s_i^2)} + \frac{1 + s_i^2}{2s_i^2\sigma_{1_i}^2} \right) + \right. \\
&\quad \left. \lambda_1 \|\mathbf{x}\|_1 + \lambda_2 \|\mathbf{x}\|_2^2 \right\} \quad \text{(Because } \operatorname{erfc} \left(\frac{\alpha_i}{\sqrt{\beta_i}} \right) \approx 2) \\
&= \arg \min \left\{ \sum_i \left(z_i + 1.5 \ln(e^{-2z_i} + s_i^2) - \ln(e^{-z_i} + s_i^2) + \frac{(1 - e^{-z_i})^2}{2\sigma_{1_i}^2(e^{-2z_i} + s_i^2)} \right) + \lambda_1 \|\mathbf{x}\|_1 + \lambda_2 \|\mathbf{x}\|_2^2 \right\}
\end{aligned} \tag{B.4}$$

The gradient of each term in (B.4) can be found as:

$$\begin{aligned}
\frac{\partial \sum z_i}{\partial \mathbf{x}} &= -\sum \mathbf{a}_i^T \\
\frac{\partial \sum \ln(e^{-2z_i} + s_i^2)}{\partial \mathbf{x}} &= \sum \frac{2e^{-2z_i}}{(e^{-2z_i} + s_i^2)} \mathbf{a}_i^T \\
\frac{\partial \sum \ln(e^{-z_i} + s_i^2)}{\partial \mathbf{x}} &= \sum \frac{e^{-z_i}}{(e^{-z_i} + s_i^2)} \mathbf{a}_i^T \\
\frac{\partial -\sum \frac{(1 - e^{-z_i})^2}{(e^{-2z_i} + s_i^2)}}{\partial \mathbf{x}} &= \sum \frac{2e^{-z_i}(1 - e^{-z_i})(s_i^2 + e^{-z_i})}{(s_i^2 + e^{-2z_i})^2} \mathbf{a}_i^T
\end{aligned}$$

Hence

$$\begin{aligned}
\nabla f(\mathbf{x}) &= -\sum_i \left(1 - \frac{3e^{-2z_i}}{(e^{-2z_i} + s_i^2)} + \frac{e^{-z_i}}{(e^{-z_i} + s_i^2)} - \frac{e^{-z_i}(1 - e^{-z_i})(s_i^2 + e^{-z_i})}{\sigma_{1_i}^2 (s_i^2 + e^{-2z_i})^2} \right) \mathbf{a}_i^T \\
&+ \lambda_1 \frac{\partial \|\mathbf{x}\|_1}{\partial \mathbf{x}} + 2\lambda_2 \mathbf{x}.
\end{aligned}$$

APPENDIX C

Implementation of the Ellipsoid Algorithm

The convergence speed of the ellipsoid algorithm discussed in CH.4 is

$$\mathbf{vol}(\mathbf{P}^{(k+1)}) < e^{-\frac{1}{2N}} \mathbf{vol}(\mathbf{P}^k),$$

where $\mathbf{vol}(\mathbf{P}^k)$ denotes the volume of a ellipsoid after k iterations, N is the number of pixels.

Hence, the volume reduction factor degrades significantly with N . It is desire to implement an efficient code to accelerate the process by incorporating some features or special structure of the matrices in the process. However, it might be a difficult task to implement such a efficient code in MATLAB. In this work, the ellipsoid algorithm was implemented in C with the BLAS library[24, 25]. Moreover, since the original data format is “.mat”, which is easier to be load in MATLAB, the C code was compiled in MATLAB with its *mex* function.

In addition to use the variables wisely, a few comments on implementing the algorithms are listed below:

1. Computing the noise vector can be simply done by using the BLAS function *dgemv*;
2. It is not necessary to compute the value of the cost function in each step as only the gradient is needed in order to proceed to next step, unless tracking the optimization progress is needed;
3. The ellipsoid matrix \mathbf{P} is a symmetric positive definite (SPD) matrix, hence its rank one downdate step in each iteration can be accelerated by the BLAS function *dsyr*. Note that, the matrix might loss its SPD property due to the round-off error. In this case, the Cholesky factorization of the ellipsoid matrix should be implement by using LAPACK and the matrix downdate step can be consequently converted into a Cholesky Rank-1 downdate step;

4. All the matrix computation steps might be accelerated by using some GPU parallel computing libraries, e.g. CUDA, especially when the matrix size is big.

REFERENCES

- [1] M.V. Afonso, J.M. Bioucas-Dias, and M.A.T. Figueiredo. Fast image recovery using variable splitting and constrained optimization. *Image Processing, IEEE Transactions on*, 19(9):2345–2356, September 2010.
- [2] W. F Ames. *Numerical methods for partial differential equations*. Academic Press, 1977.
- [3] George B Arfken and Hans-Jurgen Weber. *Mathematical methods for physicists*. Elsevier, Boston, 2005.
- [4] S R Arridge. Optical tomography in medical imaging. *Inverse Problems*, 15(2):R41, April 1999.
- [5] Simon R Arridge and John C Schotland. Optical tomography: forward and inverse problems. *Inverse Problems*, 25(12):123010, December 2009.
- [6] SR Arridge, M Schweiger, M Hiraoka, and DT Delpy. A finite element approach for modeling photon transport in tissue. *Med Phys*, 20(2 Pt 1):299–309, March 1993.
- [7] Mikhail J. Atallah and Marina Blanton, editors. *Algorithms and theory of computation handbook: general concepts and techniques*. Chapman & Hall/CRC, 2 edition, 2010.
- [8] D.A. Boas, D.H. Brooks, E.L. Miller, C.A. DiMarzio, M. Kilmer, R.J. Gaudette, and Quan Zhang. Imaging the body with diffuse optical tomography. *Signal Processing Magazine, IEEE*, 18(6):57–75, November 2001.

- [9] David Boas, J. Culver, J. Stott, and A. Dunn. Three dimensional monte carlo code for photon migration through complex heterogeneous media including the adult human head. *Opt. Express*, 10(3):159170, February 2002.
- [10] David A. Boas, Anders M. Dale, and Maria Angela Franceschini. Diffuse optical imaging of brain activation: approaches to optimizing image sensitivity, resolution, and accuracy. *NeuroImage*, 23(Supplement 1):S275–S288, September 2004.
- [11] Stephen P Boyd and Lieven Vandenberghe. *Convex optimization*. Cambridge University Press, Cambridge, UK; New York, 2004.
- [12] Alper Bozkurt, Arye Rosen, Harel Rosen, and Banu Onaral. A portable near infrared spectroscopy system for bedside monitoring of newborn brain. *BioMedical Engineering OnLine*, 4(1):29, April 2005.
- [13] E.J. Candes and M.B. Wakin. An introduction to compressive sampling. *Signal Processing Magazine, IEEE*, 25(2):21–30, November 2008.
- [14] Nannan Cao, Arye Nehorai, and Mathews Jacobs. Image reconstruction for diffuse optical tomography using sparsity regularization and expectation-maximization algorithm. *Opt. Express*, 15(21):13695–13708, October 2007.
- [15] Liang-Yu Chen, Min-Chun Pan, and Min-Cheng Pan. Implementation of edge-preserving regularization for frequency-domain diffuse optical tomography. *Applied Optics*, 51(1):43–54, January 2012.
- [16] W.F. Cheong, S.A. Prahl, and A.J. Welch. A review of the optical properties of biological tissues. *Quantum Electronics, IEEE Journal of*, 26(12):2166–2185, December 1990.
- [17] Man-Fung Cheung, S. Yurkovich, and K.M. Passino. An optimal volume ellipsoid algorithm for parameter set estimation. *IEEE Transactions on Automatic Control*, 38(8):1292–1296, 1993.

- [18] R. Choe. Diffuse optical tomography & spectroscopy in breast cancer characterization & therapy monitoring at UPENN (invited paper). In *Engineering in Medicine and Biology Society, 2009. EMBC 2009. Annual International Conference of the IEEE*, pages 6335–6337, 2009.
- [19] Regine Choe, Turgut Durduran, So Hyun Chung, Soren D. Konecky, Saurav Pathak, Han Y. Ban, David R. Busch, Erin M. Buckley, Meeri N. Kim, Angela DeMichele, Carolyn Mies, Mark A. Rosen, Mitchell D. Schnall, and Arjun G. Yodh. Breast cancer therapy monitoring with diffuse optical tomography and diffuse correlation spectroscopy. In *Biomedical Optics*, page BSubB2. Optical Society of America, 2010.
- [20] Teresa Correia, Adam Gibson, Martin Schweiger, and Jeremy Hebden. Selection of regularization parameter for optical topography. *Journal of Biomedical Optics*, 14(3):034044, March 2009.
- [21] J. P. Culver, V. Ntziachristos, M. J. Holboke, and A. G. Yodh. Optimization of optode arrangements for diffuse optical tomography: A singular-value analysis. *Optics Letters*, 26(10):701–703, May 2001.
- [22] Joseph P Culver, Turgut Durduran, Daisuke Furuya, Cecil Cheung, Joel H Greenberg, and A G Yodh. Diffuse optical tomography of cerebral blood flow, oxygenation, and metabolism in rat during focal ischemia. *J Cereb Blood Flow Metab*, 23(8):911–924, August 2003.
- [23] D T Delpy, M Cope, P van der Zee, S Arridge, S Wray, and J Wyatt. Estimation of optical pathlength through tissue from direct time of flight measurement. *Physics in Medicine and Biology*, 33(12):1433, 1988.
- [24] J. Dongarra. Preface: Basic linear algebra subprograms technical (blast) forum standard. *International Journal of High Performance Computing Applications*, 16(2):115–115, May 2002.

- [25] J. Dongarra. Preface: Basic linear algebra subprograms technical (blast) forum standard. *International Journal of High Performance Computing Applications*, 16(1):1–1, February 2002.
- [26] A. Douiri, M. Schweiger, J. Riley, and S R Arridge. Anisotropic diffusion regularization methods for diffuse optical tomography using edge prior information. *Measurement Science and Technology*, 18(1):87, November 2006.
- [27] Abdel Douiri, Martin Schweiger, Jason Riley, and Simon Arridge. Local diffusion regularization method for optical tomography reconstruction by using robust statistics. *Optics Letters*, 30(18):2439–2441, September 2005.
- [28] Turgut Durduran, Regine Choe, W Baker, and A G Yodh. Diffuse optics for tissue monitoring and tomography. *Reports on Progress in Physics*, 73(7):076701, 2010.
- [29] J. G. Ecker and M. Kupferschmid. An ellipsoid algorithm for nonlinear programming. *Mathematical Programming*, 27(1):83–106, September 1983.
- [30] Adam T. Eggebrecht, Brian R. White, Silvina L. Ferradal, Chunxiao Chen, Yuxuan Zhan, Abraham Z. Snyder, Hamid Dehghani, and Joseph P. Culver. A quantitative spatial comparison of high-density diffuse optical tomography and fMRI cortical mapping. *NeuroImage*, 61(4):1120–1128, July 2012.
- [31] Reiko Endoh, Mamiko Fujii, and Kiyoshi Nakayama. Depth-adaptive regularized reconstruction for reflection diffuse optical tomography. *Optical Review*, 15(1):51–56, March 2008.
- [32] Qianqian Fang. Mesh-based monte carlo method using fast ray-tracing in plcker coordinates. *Biomedical Optics Express*, 1(1):165–175, July 2010.
- [33] Silvina L. Ferradal, Adam T. Eggebrecht, Mahlega Hassanpour, Abraham Z. Snyder, and Joseph P. Culver. Atlas-based head modeling and spatial normal-

- ization for high-density diffuse optical tomography: In vivo validation against fMRI. *NeuroImage*, April 2013.
- [34] A. H. Gandjbakhche, G. H. Weiss, R. F. Bonner, and R. Nossal. Photon path-length distributions for transmission through optically turbid slabs. *Physical Review E*, 48(2):810–818, August 1993.
- [35] Amir H. Gandjbakhche and George H. Weiss. Random walk and diffusion-like models of photon migration in turbid media. In *Progress in Optics*, volume Volume 34, pages 333–402. Elsevier, 1995.
- [36] Richard J Gaudette, Dana H Brooks, Charles A DiMarzio, Misha E Kilmer, Eric L Miller, Thomas Gaudette, and David A Boas. A comparison study of linear reconstruction techniques for diffuse optical tomographic imaging of absorption coefficient. *Physics in Medicine and Biology*, 45(4):1051, April 2000.
- [37] A P Gibson, J C Hebden, and S R Arridge. Recent advances in diffuse optical imaging. *Physics in Medicine and Biology*, 50(4):R1, February 2005.
- [38] Gene H. Golub, Michael Heath, and Grace Wahba. Generalized cross-validation as a method for choosing a good ridge parameter. *Technometrics*, 21(2):215–223, May 1979.
- [39] I. S Gradshten, I. M Ryzhik, and A. Jeffrey. *Table of Integrals, Series, and Products*. Academic Press, 1994.
- [40] Murat Guven, Birsen Yazici, Xavier Intes, and Britton Chance. Diffuse optical tomography with a priori anatomical information. *Physics in Medicine and Biology*, 50(12):2837, June 2005.
- [41] Per Christian Hansen. Analysis of discrete ill-posed problems by means of the l-curve. *SIAM Review*, 34(4):561–580, December 1992.

- [42] Junzhou Huang and Tong Zhang. The benefit of group sparsity. *The Annals of Statistics*, 38(4):1978–2004, August 2010. Mathematical Reviews number (MathSciNet): MR2676881; Zentralblatt MATH identifier: 05774396.
- [43] An Jin, Birsen Yazici, Angelique Ale, and Vasilis Ntziachristos. Preconditioning of the fluorescence diffuse optical tomography sensing matrix based on compressive sensing. *Optics Letters*, 37(20):4326–4328, October 2012.
- [44] B. Jin and D. Lorenz. Heuristic parameter-choice rules for convex variational regularization based on error estimates, 2010.
- [45] Venkaiah C. Kavuri, Zi-Jing Lin, Fenghua Tian, and Hanli Liu. Sparsity enhanced spatial resolution and depth localization in diffuse optical tomography. *Biomedical Optics Express*, 3(5):943–957, May 2012.
- [46] S. M Kay. *Fundamentals Of Statistical Signal Processing*. Prentice Hall, 2001.
- [47] Bilal Khan, Pankaj Chand, and George Alexandrakis. Spatiotemporal relations of primary sensorimotor and secondary motor activation patterns mapped by NIR imaging. *Biomedical Optics Express*, 2(12):3367–3386, November 2011. PMID: 22162826 PMCID: PMC3233255.
- [48] Seung-Jean Kim, K. Koh, M. Lustig, S. Boyd, and D. Gorinevsky. An interior-point method for large-scale l_1 -regularized least squares. *Selected Topics in Signal Processing, IEEE Journal of*, 1(4):606–617, December 2007.
- [49] Matthieu Kowalski and Bruno Torrsani. Sparsity and persistence: mixed norms provide simple signal models with dependent coefficients. *Signal, Image and Video Processing*, 3(3):251–264, September 2009.
- [50] Okkyun Lee, Jong Min Kim, Y. Bresler, and Jong Chul Ye. Compressive diffuse optical tomography: Noniterative exact reconstruction using joint sparsity. *Medical Imaging, IEEE Transactions on*, 30(5):1129–1142, May 2011.

- [51] Yuting Lin, Dave Thayer, Orhan Nalcioğlu, and Gultekin Gulsen. Tumor characterization in small animals using magnetic resonance-guided dynamic contrast enhanced diffuse optical tomography. *Journal of Biomedical Optics*, 16(10):106015–106015–4, 2011.
- [52] M. Lustig, D.L. Donoho, J.M. Santos, and J.M. Pauly. Compressed sensing MRI. *Signal Processing Magazine, IEEE*, 25(2):72–82, March 2008.
- [53] Michael Lustig, David Donoho, and John M. Pauly. Sparse MRI: the application of compressed sensing for rapid MR imaging. *Magnetic Resonance in Medicine*, 58(6):1182–1195, October 2007.
- [54] Vadim A. Markel, Vivek Mital, and John C. Schotland. Inverse problem in optical diffusion tomography. III. inversion formulas and singular-value decomposition. *J. Opt. Soc. Am. A*, 20(5):890902, May 2003.
- [55] Vadim A. Markel, Joseph A. O’Sullivan, and John C. Schotland. Inverse problem in optical diffusion tomography. IV. nonlinear inversion formulas. *J. Opt. Soc. Am. A*, 20(5):903912, May 2003.
- [56] Vadim A. Markel and John C. Schotland. Inverse problem in optical diffusion tomography. i. fourier-laplace inversion formulas. *J. Opt. Soc. Am. A*, 18(6):13361347, June 2001.
- [57] Vadim A. Markel and John C. Schotland. Inverse problem in optical diffusion tomography. II. role of boundary conditions. *J. Opt. Soc. Am. A*, 19(3):558566, March 2002.
- [58] Lukas Meier, Sara Van De Geer, and Peter Bhlmann. The group lasso for logistic regression. *Journal of the Royal Statistical Society: Series B (Statistical Methodology)*, 70(1):5371, 2008.

- [59] Haijing Niu, Fenghua Tian, Zi-Jing Lin, and Hanli Liu. Development of a compensation algorithm for accurate depth localization in diffuse optical tomography. *Opt. Lett.*, 35(3):429–431, February 2010.
- [60] Vasilis Ntziachristos, Britton Chance, and Arjun Yodh. Differential diffuse optical tomography. *Optics Express*, 5(10):230–242, November 1999.
- [61] Vasilis Ntziachristos, A. G. Yodh, Mitchell Schnall, and Britton Chance. Concurrent MRI and diffuse optical tomography of breast after indocyanine green enhancement. *Proceedings of the National Academy of Sciences*, 97(6):2767 – 2772, March 2000.
- [62] S. Okawa, Y. Endo, Y. Hoshi, and Y. Yamada. Reduction of poisson noise in measured time-resolved data for time-domain diffuse optical tomography. *Medical & Biological Engineering & Computing*, 50(1):69–78, January 2012.
- [63] M. A. O’Leary, D. A. Boas, B. Chance, and A. G. Yodh. Experimental images of heterogeneous turbid media by frequency-domain diffusing-photon tomography. *Opt. Lett.*, 20(5):426–428, March 1995.
- [64] Maureen Ann O’Leary. *Imaging with diffuse photon density waves*. PhD thesis, University of Pennsylvania, United States – Pennsylvania, 1996. Ph.D.
- [65] B W Pogue, M S Patterson, H. Jiang, and K D Paulsen. Initial assessment of a simple system for frequency domain diffuse optical tomography. *Physics in Medicine and Biology*, 40(10):1709, October 1995.
- [66] Brian W. Pogue, Troy O. McBride, Judith Prewitt, Ulf L. sterberg, and Keith D. Paulsen. Spatially variant regularization improves diffuse optical tomography. *Applied Optics*, 38(13):2950–2961, May 1999.
- [67] E. Scherleitner and B.G. Zagar. Optical tomography imaging based on higher order born approximation of diffuse photon density waves. *Instrumentation and Measurement, IEEE Transactions on*, 54(4):1607– 1611, August 2005.

- [68] Martin Schweiger, Simon R. Arridge, Mutsuhisa Hiraoka, Michael Firbank, and David T. Delpy. Comparison of a finite-element forward model with experimental phantom results: application to image reconstruction. In Britton Chance and Robert R. Alfano, editors, *Photon Migration and Imaging in Random Media and Tissues*, volume 1888, pages 179–190. SPIE, 1993.
- [69] Xiaomei Song, Brian W. Pogue, Shudong Jiang, Marvin M. Doyley, Hamid Dehghani, Tor D. Tosteson, and Keith D. Paulsen. Automated region detection based on the contrast-to-noise ratio in near-infrared tomography. *Applied Optics*, 43(5):1053–1062, February 2004.
- [70] Mehmet Szen, Alexia Giannoula, and Turgut Durduran. Compressed sensing in diffuse optical tomography. *Optics Express*, 18(23):23676–23690, November 2010.
- [71] Behnoosh Tavakoli and Quing Zhu. Depth-correction algorithm that improves optical quantification of large breast lesions imaged by diffuse optical tomography. *Journal of Biomedical Optics*, 16(5):056002, May 2011.
- [72] Fenghua Tian, George Alexandrakis, and Hanli Liu. Optimization of probe geometry for diffuse optical brain imaging based on measurement density and distribution. *Applied Optics*, 48(13):2496–2504, May 2009.
- [73] Fenghua Tian, F Andrew Kozel, Amarnath Yennu, Paul E Croarkin, Shawn M McClintock, Kimberly S Mapes, Mustafa M Husain, and Hanli Liu. Test-retest assessment of cortical activation induced by repetitive transcranial magnetic stimulation with brain atlas-guided optical topography. *Journal of biomedical optics*, 17(11):116020, November 2012. PMID: 23139044.
- [74] Fenghua Tian, Haijing Niu, Sabin Khadka, Zi-Jing Lin, and Hanli Liu. Algorithmic depth compensation improves quantification and noise suppression in

- functional diffuse optical tomography. *Biomedical Optics Express*, 1(2):441–452, September 2010.
- [75] A Tikhonov. Solution of incorrectly formulated problems and the regularization method. In *Soviet Math. Doklady*, volume 4, pages 1035–1038, 1963.
- [76] Vlad Toronov, Enrico D’Amico, Dennis Hueber, Enrico Gratton, Beniamino Barbieri, and Andrew Webb. Optimization of the signal-to-noise ratio of frequency-domain instrumentation for near-infrared spectro-imaging of the human brain. *Optics Express*, 11(21):2717–2729, October 2003.
- [77] C. R Vogel. *Computational methods for inverse problems*. Society for Industrial and Applied Mathematics, 2002.
- [78] Zhou Wang, A.C. Bovik, H.R. Sheikh, and E.P. Simoncelli. Image quality assessment: from error visibility to structural similarity. *IEEE Transactions on Image Processing*, 13(4):600–612, 2004.
- [79] Phaneendra K. Yalavarthy, Brian W. Pogue, Hamid Dehghani, and Keith D. Paulsen. Weight-matrix structured regularization provides optimal generalized least-squares estimate in diffuse optical tomography. *Medical Physics*, 34(6):2085–2098, June 2007.
- [80] Jixing Yao, Fenghua Tian, Soontorn Orintara, and Hanli Liu. Novel method to improve 2D DOT spatial resolution using l1-regularization and noise-normalization. In *Biomedical Optics*, page BTu3A.34, 2012.
- [81] Qing Zhao, Lijun Ji, and Tianzi Jiang. Improving depth resolution of diffuse optical tomography with a layer-based sigmoid adjustment method. *Opt. Express*, 15(7):4018–4029, April 2007.
- [82] Hui Zou and Trevor Hastie. Regularization and variable selection via the elastic net. *Journal of the Royal Statistical Society: Series B (Statistical Methodology)*, 67(2):301320, 2005.

- [83] Anna Zourabian, Andy Siegel, Britton Chance, Nirmala Ramanujam, Martha Rode, and David A. Boas. Trans-abdominal monitoring of fetal arterial blood oxygenation using pulse oximetry. *Journal of Biomedical Optics*, 5(4):391–405, October 2000.

BIOGRAPHICAL STATEMENT

Jixing Yao earned his B.E. degree in telecommunication engineering from Huaqiao University (HQU), Fujian, China in 2007. He received the M.S. degree in electrical engineering from Louisiana Tech University, Ruston, LA in 2010. His research interests are in the area of signal processing, compressive sensing, medical imaging, inverse problem, and statistical noise modeling. He is a member of the Institute of Electrical and Electronics Engineers (IEEE) and golden key international honor society.